Redox Biology 54 (2022) 102384

Contents lists available at ScienceDirect

Redox Biology

journal homepage: www.elsevier.com/locate/redox

# Notoginsenoside R1-loaded mesoporous silica nanoparticles targeting the site of injury through inflammatory cells improves heart repair after myocardial infarction

Han Li [a,b,1], Jing Zhu [b,1], Yan-wu Xu [c,1], Fang-fang Mou [b], Xiao-li Shan [d], Qiang-li Wang [e], Bao-nian Liu [b], Ke Ning [f], Jia-jia Liu [a,b], Ya-chao Wang [a,b], Jin-xia Mi [g], Xiaohui Wei [h], Shui-jin Shao [b], Guo-hong Cui [i,***], Rong Lu [d,**], Hai-dong Guo [a,b,*]

[a] Academy of Integrative Medicine, Shanghai University of Traditional Chinese Medicine, Shanghai, 201203, China
[b] Department of Anatomy, School of Basic Medicine, Shanghai University of Traditional Chinese Medicine, Shanghai, 201203, China
[c] Department of Biochemistry, School of Basic Medicine, Shanghai University of Traditional Chinese Medicine, Shanghai, 201203, China
[d] School of Basic Medicine, Shanghai University of Traditional Chinese Medicine, Shanghai, 201203, China
[e] Department of Histoembryology, School of Basic Medicine, Shanghai University of Traditional Chinese Medicine, Shanghai, 201203, China
[f] Department of Physiology, School of Basic Medicine, Shanghai University of Traditional Chinese Medicine, Shanghai, 201203, China
[g] Science and Technology Center, Shanghai University of Traditional Chinese Medicine, Shanghai, China
[h] The MOE Key Laboratory for Standardization of Chinese Medicines and the SATCM Key Laboratory for New Resources and Quality Evaluation of Chinese Medicines, Institute of Chinese Materia Medica, Shanghai University of Traditional Chinese Medicine, Shanghai, 201203, China
[i] Department of Neurology, Shanghai No. 9 People's Hospital, Shanghai Jiaotong University School of Medicine, Shanghai, 200011, China

## ARTICLE INFO

*Keywords:*
Myocardial infarction
Notoginsenoside R1
Mesoporous silica nanoparticles
PI3K/AKT signaling pathway
MAPK signaling pathway
Hippo signaling pathway
Targeting

## ABSTRACT

Notoginsenoside R1 (NGR1) is the main monomeric component extracted from the dried roots and rhizomes of Panax notoginseng, and exerts pharmacological action against myocardial infarction (MI). Owing to the differences in compound distribution, absorption, and metabolism *in vivo*, exploring a more effective drug delivery system with a high therapeutic targeting effect is crucial. In the early stages of MI, CD11b-expressing monocytes and neutrophils accumulate at infarct sites. Thus, we designed a mesoporous silica nanoparticle-conjugated CD11b antibody with loaded NGR1 (MSN-NGR1-CD11b antibody), which allowed NGR1 precise targeted delivery to the heart in a noninvasively manner. By increasing targeting to the injured myocardium, intravenous injection of MSN-NGR1-CD11b antibody nanoparticle in MI mice improved cardiac function and angiogenesis, reduced cell apoptosis, and regulate macrophage phenotype and inflammatory factors and chemokines. In order to further explore the mechanism of NGR1 protecting myocardium, cell oxidative stress model and oxygen-glucose deprivation (OGD) model were established. NGR1 protected H9C2 cells and primary cardiomyocytes against oxidative injury induced by $H_2O_2$ and OGD treatment. Further network pharmacology and molecular docking analyses suggested that the AKT, MAPK and Hippo signaling pathways were involved in the regulation of NGR1 in myocardial protection. Indeed, NGR1 could elevate the levels of *p*-Akt and *p*-ERK, and promote the nuclear translocation of YAP. Furthermore, LY294002 (AKT inhibitor), U0126 (ERK1/2 inhibitor) and Verteporfin (YAP inhibitor) administration in H9C2 cells indicated the involvement of AKT, MAPK and Hippo signaling pathways in NGR1 effects. Meanwhile, MSN-NGR1-CD11b antibody nanoparticles enhanced the activation of AKT and MAPK signaling pathways and the nuclear translocation of YAP at the infarcted site. Our research demonstrated that MSN-NGR1-CD11b antibody nanoparticle injection after MI enhanced the targeting of NGR1 to the infarcted myocardium and improved cardiac function. More importantly, our pioneering research provides a new strategy for targeting drug delivery systems to the ischemic niche.

* Corresponding author. Academy of Integrative Medicine, Shanghai University of Traditional Chinese Medicine, Shanghai, 201203, China.
** Corresponding author.
*** Corresponding author.
*E-mail addresses:* gh_cui@qq.com (G.-h. Cui), lurong@shutcm.edu.cn (R. Lu), hdguo@shutcm.edu.cn (H.-d. Guo).
[1] These authors contributed equally to this work.

https://doi.org/10.1016/j.redox.2022.102384
Received 22 May 2022; Received in revised form 20 June 2022; Accepted 21 June 2022
Available online 24 June 2022

## 1. Introduction

Myocardial infarction (MI) is myocardial necrosis caused by acute and persistent ischemia and hypoxia of the coronary artery. To date, cardiovascular disease has accounted for more than one-third of global deaths, making MI a pressing issue in medicine today [1]. Most of the first-line MI pharmacological treatments in clinics are focused on delaying the disease process, but have little effect on rebuilding myocardial cell injury. Therefore, it is important to develop effective strategies for MI treatment.

Myocardial cell apoptosis, in which an imbalance in oxidative stress is a significant contributor, is the primary form of myocardial damage during MI [2]. Internal oxidative damage resulting from the production and accumulation of large amounts of reactive oxygen species (ROS) enhances myocardial impairment. ROS alter the properties of the cell membrane, leading to the infiltration of cardiac enzymes into the cytoplasm, which further aggravates damage to the myocardium [3]. Therefore, oxidative stress control is essential for improving cardiac function in MI.

Some herbal compounds can inhibit apoptosis and inflammatory responses in cardiomyocytes, promote myocardial angiogenesis, reduce cardiac dysfunction, and attenuate cardiac remodeling [4–7]. Notoginsenoside R1 (NGR1, chemical formula is shown in Fig. S1) has significant therapeutic effects on cardiovascular diseases; however, its oral utilization is extremely low [8], which is accounted for by its poor membrane permeability and rapid bile excretion [9].

Recently, nanomaterials have received increasing attention in the fields of drug delivery, diagnostics, therapy, medical imaging, and engineering. Nanoparticle systems are used to improve the physicochemical properties and enhance the bioavailability of drugs [10–14]. Mesoporous silica nanoparticle (MSN) drug delivery is a safe candidate for targeted treatment. Notably, MSNs can effectively load drugs as a result of their large specific surface area and pore volume [15]. MSNs also have a mesoporous structure and adjustable pore size, making it possible to load and release drugs flexibly [16]. Specifically, the surface of MSNs can be easily modified. In addition, MSNs have excellent advantages in terms of cytotoxicity [17–19], biodegradation, and excretion [20,21]. In the early stages of MI, both cell death and tissue damage appear at the infarct site. Numerous immune cells infiltrate to the infarct site and induce a solid inflammatory response, which further prompts the accumulation of CD11b-expressing monocytes and neutrophils to the infarct site [22]. In our research, coupling CD11b antibodies to NGR1-equipped MSNs allowed NGR1 to target the infarcted heart area for effective therapeutic action.

We loaded NGR1 into MSNs, which had a modified CD11b antibody on their surface, and injected them into MI mice to evaluate their effects on MI. The network pharmacology and molecular docking analyses was performed to explore the underlying mechanisms. The cardiomyocyte injury model with $H_2O_2$ or oxygen-glucose deprivation (OGD) to simulate the ischemic-hypoxic microenvironment after MI was established *in vitro*.

## 2. Materials and methods

### 2.1. Preparation of the nanoprobe

Carboxyl-modified mesoporous silica with an indocyanine green (ICG) mixture was diluted with phosphate buffered saline (PBS) solution (0.02 M, pH = 7.4) and centrifuged. The supernatant was collected, and 100 μg of 1-(3-Dimethylaminopropyl)-3-ethylcarbodiimide (EDC) and 1 mg of NGR1 were added to make a solution, which was then shaken overnight. On the second day, the supernatant was collected from the shaken solution after centrifugation. Next, 50 μg EDC and 50 μg CD11b monoclonal antibody (Functional grade, Invitrogen) were added before shaking overnight. On the third day, the supernatant was collected after centrifugation and stored at 4 °C.

### 2.2. Drug loading rate and antibody coupling rate

The concentration of NGR1 in the supernatant was measured using an ultraviolet visible spectrophotometer (UV-1780, Shimadzu, Japan), and the ultraviolet spectrum and concentration standard curve were obtained. The entrapment efficiency and drug loading rate of NGR1 were calculated. The concentration of CD11b antibody in the supernatant was measured using a microspectrophotometer (Nano-300, Aosheng Instrument, China), and the antibody coupling rate was measured.

### 2.3. Dynamic laser light scattering detection of hydrodynamic size and zeta potential distribution before and after coupling CD11b antibody on the surface of mesoporous silicon

Unconjugated CD11b antibody and CD11b antibody-conjugated mesoporous silica solutions were prepared for dynamic laser light scattering (DLS; Zeta Plus, Brookhaven Instruments). DLS was used to observe the hydrodynamic size and zeta potential distribution, from which, we could determine whether the CD11b antibody was coupled to the mesoporous silicon surface. This experiment was repeated thrice.

### 2.4. Transmission electron microscopy detection of mesoporous silicon carrying NGR1 and ICG and morphological changes before and after coupling with CD11b antibody on the surface

To perform transmission electron microscopy (TEM), 1 mL of NGR1 loaded and CD11b antibody-coupled MSN (MSN-NGR1-CD11b antibody) nanoparticles was dropped onto a copper mesh and dried naturally. The morphological changes of MSN before and after coupling with CD11b antibody and loading with NGR1 were observed and photographed under a TCM (JEM-2100, JEOL, Japan).

### 2.5. Maximum ultraviolet absorption and fluorescence spectroscopy detection of ICG

The maximum ultraviolet absorption and fluorescence spectrum of ICG were detected using an ultraviolet visible spectrophotometer and a fluorescence spectrometer (FLuoroMax-4, HORIBA, France), respectively, to verify whether the sample contained the fluorescent molecule ICG.

### 2.6. Animals

BALB/c nude mice (6 w), C57BL/6 mice (6 w), and Zsgreen transgenic mice (Gempharmatech, China) were bred at the Experimental Animal Center of Shanghai University of Traditional Chinese Medicine. The CAG promoter was used to drive the overexpression of the Zsgreen coding sequence in mice. The living environment of the mice was maintained under a 12-h light/dark cycle, with free access to water and food. The protocol was approved by the Animal Ethics Committee of the Shanghai University of Traditional Chinese Medicine and the Shanghai Animal Research Committee. We attempted to minimize animal suffering and the number of rats used during the experimental procedure.

### 2.7. Generation of MI model

After anesthesia with 0.4 L/min isoflurane gas, the chest of each mouse was opened laterally with its heart exposed under sterile conditions. The left anterior descending coronary artery, 2–3 mm below the starting point, was ligated. Finally, the chest cavity was closed, air was extruded from the chest cavity, and the skin incision was sutured. After spontaneous breathing restoration, the cannula of each mouse was removed and machine-assisted breathing was stopped.

After MI surgery, C57BL-6 mice were randomly divided into the Sham, MI, MSN-NGR1, and MSN-NGR1-CD11b antibody groups. Mice in

the MSN-NGR1 and MSN-NGR1-CD11b antibody groups were administered MSN-NGR1 or MSN-NGR1-CD11b antibodies, respectively, at a single dose of 267 ng/kg via the caudal vein 24 h after MI. Mice in the Sham group and MI group were injected with MSN-NGR1-CD11b antibodies nanoparticles and normal saline, respectively. To compare the cardioprotective effects between MSN-NGR1-CD11b nanoparticles and regular NGR1 treatment without nanoparticles, NGR1 without nanoparticles was administrated by two ways: intragastric administration and intravenous injection. The dosage of intravenous injection was the same as MSN-NGR1 nanoparticles, while the dosage of intragastric administration was 40 mg/kg according to the literatures. To be consistent with MSN-NGR1-CD11b nanoparticles injection, NGR1 without nanoparticles was intragastric administrated and intravenous injected only once, respectively.

### 2.8. In vivo imaging detection

For *in vivo* imaging, MSN-NGR1-CD11b antibody was injected into BALB/c nude mice with or without MI. The fluorescent ICG molecule was observed and photographed at 3, 6, 12, 24, and 48 h after injection using a small animal live imager (PerkinElmer, PE IVIS, USA).

### 2.9. Extraction of CD11b positive cells from the peripheral blood of zsgreen mice

Blood was collected from the heart of Zsgreen mice after MI surgery. Blood was incubated on ice for 15 min with ammonium chloride solution (STEMCELL Technologies, 07800, Canada). After centrifugation, the supernatant was discarded and the cells were washed with RoboSep™ Buffer (STEMCELL Technologies, 20104, Canada) and resuspended. Subsequently, the sample was transferred to a polystyrene round-bottom tube with 25 μL normal rat serum (Abcam, ab13551, USA) and 25 μL selection cocktail (STEMCELL Technologies, 14766, Canada) in each well, and the sample was incubated at room temperature for 5 min. RapidSpheres™ (40 μL/1 mL) and RoboSep™ buffer were added to the sample and the tube was placed in an EasySep™ magnet (STEMCELL Technologies, 18000, Canada) at room temperature for 3 min. After removing the supernatant from the tube in the magnet, the cells were resuspended in sterile PBS. The harvested cells were injected into BALB/c nude mice with or without MI.

### 2.10. Echocardiography

Transthoracic echocardiography was performed using a Vevo 2100 Imaging System (VisualSonics, USA) after 4 weeks of treatment. An M-mode image of the left ventricle in the parasternal long-axis view was captured.

### 2.11. Masson's trichrome staining

To assess collagen deposition and the size of the infarct area, 10-μm myocardial tissue sections were stained with modified Masson's trichrome staining solution (BP-DL022, Sbjbio, China) and observed under a microscope (IX53, Olympus).

### 2.12. Network pharmacological analysis of possible mechanisms of NGR1 against MI

Different format structure files of NGR1 were obtained from PubChem. Then, their bioinformatic targets were collected in a dataset after searching the websites of ETCM, BATMAN-TCM, PharmMapper, ChemMapper, and Swiss Target Prediction. The MI-related gene dataset was prepared from TTD, CTD, DisGeNET, Phenopedia, and PHARMGKB. The intersecting genes of these two datasets were considered potential targets for NGR1 treatment in MI. These intersecting genes were optimized using STRING and Cytoscape software to generate a drug-target-disease network.

Then, a protein-protein (PPI) network of the intersection genes mentioned above was successively screened according to degree centrality (DC) or betweenness centrality (BC) using the Cytoscape plug-in BisoGenet. The regulation of genes in the core PPI network is considered the main agent for the therapeutic effect of NGR1. Gene ontology (GO) function analysis and Kyoto Encyclopedia of Genes and Genomes (KEGG) enrichment analysis of the core network genes were performed using R software.

### 2.13. Molecular docking of drugs with key proteins in signaling pathways of interest

Molecular docking was used to further explore the possibility of drug regulation of key proteins in the signaling pathway of interest. The structure file of the protein (receptor) was downloaded from RCSB PDB, and AutoDock Vina 1.1.2 was used to evaluate the binding energy of the ligand and receptor. A binding energy $\leq -7.0$ kcal/mol was considered to indicate strong binding ability [23]. The PYMOL software was used to visualize the optimal binding mode.

### 2.14. Cell culture

H9C2 cells were cultured in Gibco Dulbecco's Modified Eagle Medium (DMEM) medium (iCell-128-0001, iCell, Shanghai, China) supplemented with 10% fetal bovine serum (FBS; 16140071, Thermo Fisher, USA), and 1% penicillin streptomycin solution (30-002-Cia, Corning Cellgro, China) at 37 °C in a humidified incubator containing 5% $CO_2$ and 95% air. Primary cultured neonatal cardiomyocyte was reserved from P 0 rats. Briefly, all apex of heart were separated from the sacrificial rats, and washed in HBSS. The tissue was digested successively for 5 times by 0.1% II collagenase (abs47048001, absin, Shanghai, China) and maintained in a DMEM medium with 10% FBS until assay. Adult C57BL/6 mice (six weeks old) were used for adult cardiomyocytes isolation. Briefly, mice were euthanized and their hearts were harvested. Then the hearts were perfused with Tyrode's solution until the color of hearts turns pale, followed by digestion solution (Collagenase Type II) for 30 min. Single cell suspension was transferred to a culture plate for 30 min and supernatant containing non-myocytes were separated. Then, the cells were resuspended with compound calcium solution for three times. After that, the cells were seeded in laminin pre-coated plates and the culture medium was replaced into MEM containing 2 mM L-glutamine, 1.26 mM CaCL2, 10% FBS, 1% penicillin/streptomycin and 10 mM 2,3-Butanedione 2-monoxime after 2 h for further assay.

### 2.15. $H_2O_2$ damage and OGD model

After 24 h of culture, H9C2 cells were induced with a 0–1000 μM gradient of $H_2O_2$ (323381, Sigma-Aldrich, USA) for 2 h, of which 350 μM (mortality rate ≈50%) was used to establish the cardiomyocyte injury model for the following cell experiments.

To create an OGD environment, H9C2 cells or primary cultured cardiomyocytes were refreshed with glucose-free DMEM in an anaerobic chamber filled with 95% $N_2$ and 5% $CO_2$. To explore the mechanisms, H9C2 cells were treated with 25 μM LY294002 (AKT inhibitor, Selleck, USA), 10 μM U0126 (ERK1/2 inhibitor, Selleck, USA) or 5 μM Verteporfin (VP; YAP inhibitor, Selleck, USA) at 30 min before NGR1 treatment.

### 2.16. CCK-8 assay

Cell viability of H9C2 cells and primary cardiomyocytes was measured using a Cell Counting kit-8 (CCK-8) assay (40203ES88, YEASEN, Shanghai, China). Briefly, 10 μL of detection reagent was added to each well of the culture plate. After 1.5 h incubation, the optical density (OD) at 450 nm was measured using a microplate reader (Synergy 2, Bio-

Tek, USA).

### 2.17. Annexin V-PI double staining assay

Apoptosis of H9C2 cells and primary cardiomyocytes was detected using the Annexin V-PI double staining assay (FITC Annexin V Apoptosis Detection Kit I, 556547, BD, USA). Briefly, cells were resuspended in binding buffer and incubated with 5 μL FITC Annexin V and 5 μL PI for 15 min. Finally, the binding buffer was added to each flow tube, and the cell suspension was analyzed by flow cytometry (CytoFlex S, USA) within 1 h.

### 2.18. Evaluation of oxidative stress

#### 2.18.1. ROS assay

ROS concentrations were measured using a ROS kit (S003S, Beyotime, Suzhou, China). DCFH-DA dilution (1:1000) was added to each well of the culture plate after cell treatment, and incubated for a further 20 min. The cells were observed under a fluorescence microscope (3J10254; Olympus, Tokyo, Japan).

### 2.19. Mitochondrial superoxide measurement

Mitochondrial ROS expression was measured with MitoSOX Red (M36008, Thermo, USA) following instruction. Briefly, H9C2 cells were seeded in 96-well plates with a density of $5 \times 10^4$/ml or adult primary cardiomyocytes (with physiologic stimuli by10 nmol/L isoproterenol) were seeded in 35 mm culture dishes with a density of $1 \times 10^4$/ml. After $H_2O_2$ administration, cells were incubated with 5 mmol/L MitoSOX Red probe for 10 min at 37 °C. Then the cells were washed twice with HBSS, and red fluorescence was observed under a microscope (IX53, Olympus).

### 2.20. Oxidative DNA damage

H9C2 cells were incubated with 8-oxoG antibody (sc-130914, 1:50, Santacruz, USA), followed by Donkey anti-mouse IgG (H + L) high cross-adsorbed secondary antibody (A-31570, 1:800, Thermo, USA) and the positive cells were observed through fluorescence microscope (IX53, Olympus).

### 2.21. JC-1 staining

The H9C2 cells were inoculated in 6-well plates, and used for measuring mitochondrial membrane potential. The mitochondrial membrane potential was measured by a JC-1 Mitochondrial Membrane Potential kit (40706ES60, Yeasen, Shanghai, China). The cells were washed with 0.01 M PBS and incubated with JC-1 buffer for 20 min at room temperature followed by JC-1 washing solution. Then, a fluorescence microscope was used to capture the pictures and calculate the ratio of the red–green fluorescence.

### 2.22. Western blot

The total protein concentrations of cell or tissue proteins were measured using the BCA protein assay (P0010S, Beyotime, Shanghai, China). Cytoplasmic and nuclear proteins were isolated using the Nuclear and Cytoplasmic Protein Extraction Kit (Boster, Beijing, China) according to the manufacturer's instructions. After electrophoresis and transmembrane electrophoresis, the proteins were blocked with 5% skim milk for 1 h. Then, the proteins were incubated with GAPDH (1:1000, CST, USA), *p*-AKT (1:1000, CST, USA), AKT (1:2000, CST, USA), *p*-ERK1/2 (1:2000, CST, USA), ERK1/2 (1:2000, CST, USA), FoxO4 (1:1000, Proteintech, USA), YAP (1:2000, CST, USA), LC3B (1:1000, Abcam, Cambridge, UK), and Beclin-1 (1:1000, Abcam, Cambridge, UK) antibody separately overnight at 4 °C. The next day, proteins were incubated with the corresponding horseradish peroxidase (HRP)-conjugated secondary antibody (7074S; CST, USA) and observed using enhanced chemiluminescence (WBKLS0100; Merck Millipore, USA). The OD of the reaction zone was quantified using ImageJ image analysis software (NIH, Bethesda, MD, USA).

## 3. TUNEL

Cell apoptosis was observed using terminal deoxynucleotidyl transferase-mediated dUTP nick-end labeling (TUNEL) staining (C1086, Beyotime, China). After washing with PBS, the cells or frozen sections were incubated with 0.3% Triton-X100 at room temperature for 5 min. Subsequently, the reagents of the TUNEL detection kit were mixed and incubated with samples at 37 °C for 1 h according to construction.

### 3.1. Immunofluorescence staining

Sections were blocked with normal goat serum for 30 min and incubated with the following primary antibodies overnight at 4 °C: anti-CD11b (ab8878, Abcam, Cambridge, UK), anti-CD31 (ab222783, Abcam, Cambridge, UK), anti-cTnT (ab8295, Abcam, Cambridge, UK), anti-CD86 (ab119857, Abcam, Cambridge, UK), anti-Arg-1 (16001-1-AP, Proteintech, USA), anti-*p*-AKT (4060S, CST, USA), anti-*p*-ERK1/2 (8544S, CST, USA), anti-YAP (4912S, CST, USA), anti-SERCA2a (ab3625, Abcam, Cambridge, UK), anti-*p*-Phospholamban (*p*-PLB; ab15000, Abcam, Cambridge, UK) and anti-CD206 (18704-1-AP, Proteintech, USA). The next day, the sections were incubated with goat anti-rabbit IgG Alexa Fluor 488 or goat anti-rat IgG Alexa Fluor 555 (CST, USA) for 1 h at 37 °C. After incubation, the sections were sealed with VECTASHIELD® Antifade Mounting Medium with DAPI (H-1200-10, Vector Laboratories, Burlingame, CA, USA) and observed under a microscope (IX53, Olympus).

### 3.2. Enzyme-linked immunosorbent assay

The levels of IL-6, IL-10, IL-1β, tumor necrosis factor-α (TNF-α), vascular endothelial growth factor (VEGF), basic fibroblast growth factor (bFGF), monocyte chemoattractant protein-1 (MCP-1), stem cell factor (SCF) and stromal cell derived factor-1 (SDF-1) were assessed by specific enzyme-linked immunosorbent assay kits (ml063159, ml002285, ml063132, ml002095, m1002076, m1037702, m1037840, m1063287, m1037712; Shanghai Enzyme Linkage Biotech, Shanghai, China) using extracted myocardial tissue proteins.

### 3.3. Statistical analysis

Data were statistically analyzed using GraphPad Prism 9 and are expressed as the mean ± standard deviation. Statistical tests were performed among the groups using one-way ANOVA followed by Scheffe's post hoc multiple-comparison or a Student's t-test was used for 2-groups. Statistical significance was set at $P < 0.05$.

## 4. Results

### 4.1. Successful construction of MSN-NGR1-CD11b antibody nanoparticles

MSNs coupled to CD11b antibody on the surface, and loaded with fluorescent ICG and NGR1, were designed and prepared. The entrapment efficiency and drug-loading rate of NGR1 in MSN-NGR1-CD11b antibody nanoparticles were 50.25% and 12.56%, respectively (Fig. S2). After modification by the CD11b antibody, the hydrated particle size increased from 57 nm to 83 nm (average of three measurements), while the Zeta potential increased from −46.1 mV to −32.5 mV (Fig. 1A and B). These results proved that the CD11b antibodies were successfully modified in the MSNs.

MSNs have a highly ordered mesoporous structure with well-

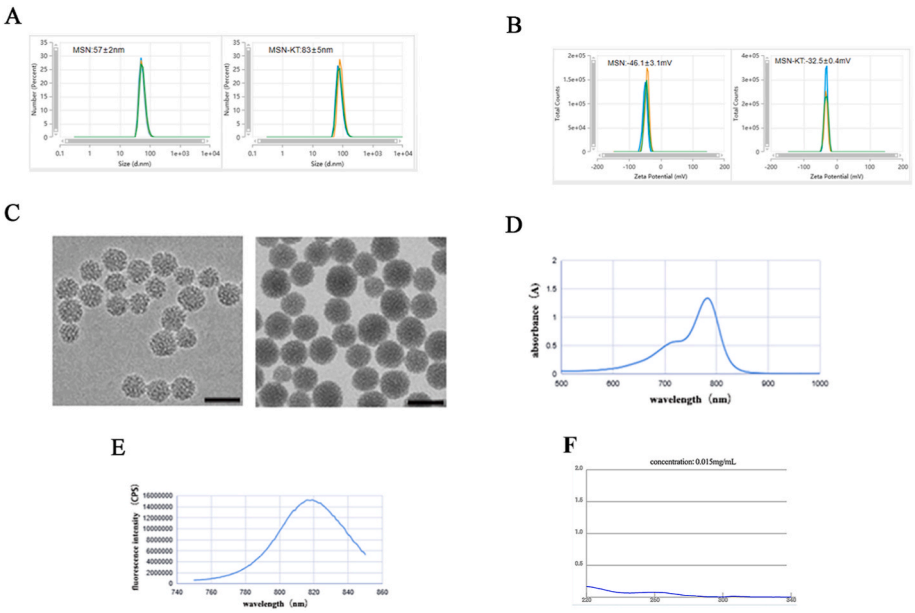


**Fig. 1.** Characterization of mesoporous silica nanoparticle-conjugated CD11b antibody with loaded NGR1 (MSN-NGR1-CD11b) and their recruitment to the infarct site. Hydrodynamic size distribution before and after coupling CD11b antibody on the mesoporous silicon surface (A). Zeta potential distribution before and after coupling CD11b antibody on the mesoporous silicon surface (B). Transmission electron microscopy (TEM) images of MSN before and after loading NGR1 and ICG and coupling CD11b antibody on the surface (C). The maximum ultraviolet absorption (D) and fluorescence spectra (E) of MSN before and after loading NGR1 and ICG and coupling CD11b antibody on the surface. Microspectrophotometer measurements for CD11b antibody coupling rate (F).

dispersed surface mesopores and a relatively homogeneous particle size before modification with antibodies. After antibody coupling, the nanoparticles still had good dispersion, and the particle size was uniform and increased. The surface and edge of the nanoparticles became blurred, and the mesopores disappeared, indicating successful modification of the antibody (Fig. 1C). According to the ultraviolet and fluorescence spectra, the maximum ultraviolet absorption peak of the sample was at 783 nm, while the maximum emission peak of the fluorescence spectrum was at 816 nm (Fig. 1D and E). According to microspectrophotometer measurements, there was 15 μg antibody in the supernatant. As the total antibody given was 50 μg, so the CD11b antibody coupling rate was 70% (Fig. 1F). The results showed that the sample contained the fluorescent ICG molecule. NGR1, ICG, and CD11b antibodies were successfully loaded into the pores or on the surface of the mesoporous silica.

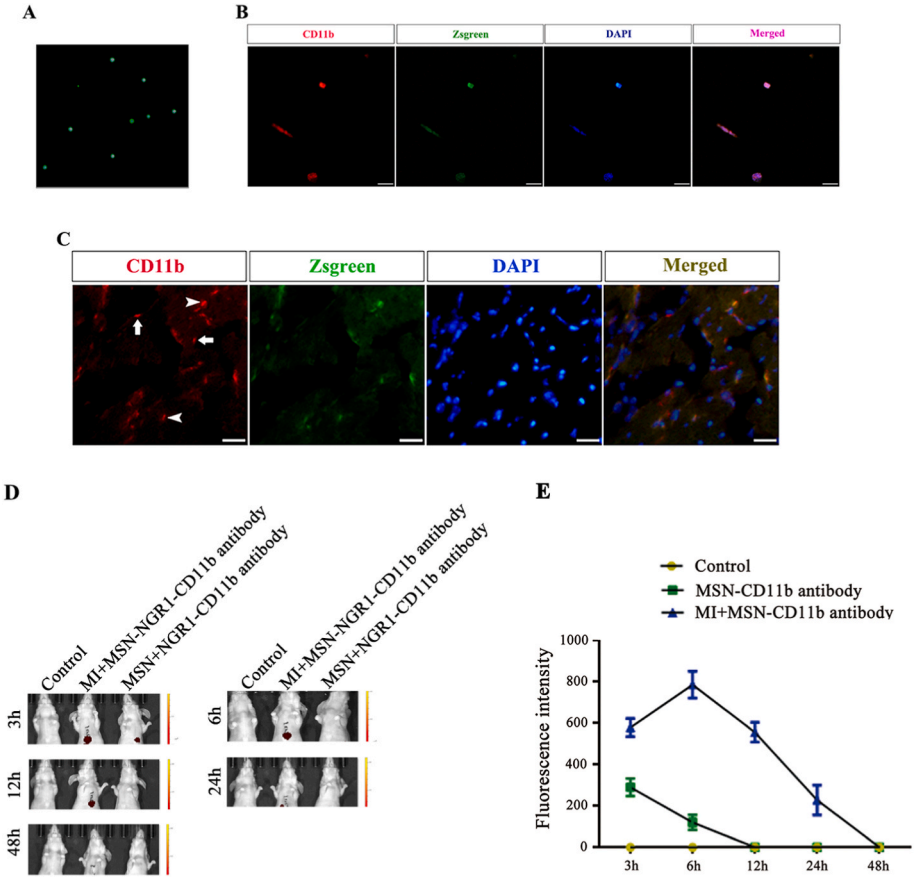


**Fig. 2.** Aggregation of CD11b + cells at the site of injury after myocardial infarction and target of MSN-NGR1-CD11b antibody nanoparticles to the MI site. Single nucleated cells isolated from the peripheral blood of Zsgreen mice (A). Isolated cells from the peripheral blood of Zsgreen mice expressing CD11b (B). Some CD11b + cells at the infarcted site were overlapped with intravenously injected Zsgreen-positive cells (arrowhead, C). Arrows showing an absence of injected Zsgreen-positive cells. Scale bar: 50 μm. *In vivo* imaging photograph of MSN-NGR1 nanoparticles after tail vein injection (D). The fluorescence intensity of *in vivo* imaging photographs (E).

### 4.2. Target of MSN-NGR1-CD11b antibody nanoparticles to the MI site

Next, we firstly verify the targeting of MSN-NGR1-CD11b antibody nanoparticles to the site of myocardial injury. During the early stages of MI, neutrophils and monocytes infiltrate and accumulate at the site of injury. To define the derivation of inflammatory cells, $CD11b^+$ cells were harvested from Zsgreen transgenic mice (Fig. 2A and B) and injected into MI mice. The hearts of MI mice were obtained 12 h after injection, and $CD11b^+$ cells were observed. We found a prominent infiltration of $CD11b^+$ cells at the infarct site, and most of the positive cells were injected with Zsgreen-positive cells (Fig. 2C). This result indicates that most of the cells infiltrating and aggregating at the injury site of the heart after MI were from the peripheral blood. Thus, $CD11b^+$ cells may be an effective means for targeting the delivery of substances to the site of the injured myocardium.

The *in vivo* imaging indicated that more MSN-NGR1-CD11b antibody nanoparticles aggregated at the heart site from 3 to 12 h compared to the control group. Indeed, MSN-NGR1-CD11b antibody nanoparticles could not target the heart without myocardial injury, and the fluorescence was quenched from 24 h after injection (Fig. 2D and E). These results demonstrated the targeting effect at the site of the injured myocardium.

### 4.3. Intravenous injection of MSN-NGR1-CD11b antibody nanoparticles improve cardiac function of mice after MI

As the MSN-NGR1-CD11b antibody nanoparticles can effectively target the site of myocardial injury after intravenous injection, the small animal echocardiography was used 4 weeks later to evaluate the changes of heart function. MI mice were divided into Sham, MI, MSN-NGR1, and MSN-NGR1-CD11b antibody groups. Compared to the MI and MSN-NGR1 groups, the ejection fraction (EF) and fractional shortening (FS) values of MI mice from the MSN-NGR1-CD11b antibody group were increased (Fig. 3A–C), as were the left ventricular end-diastolic dimension (LVEDd), left ventricular end-systolic dimension (LVEDs), left ventricular end-diastolic volume (LVEDV), and left ventricular end-diastolic volume (LVESV) values (Fig. S3, Table S1).

The infarct area, collagen deposition and ventricular wall thickness of infarcted area were determined by Masson's trichrome staining. The ventricular wall thickness of MI mice in the MSN-NGR1 and MSN-NGR1-CD11b groups was higher than that in the MI group, and was higher in the MSN-NGR1-CD11b group than in the MSN-NGR1 group. In addition, compared to the MI and MSN-NGR1 groups, the infarct area and collagen deposition in MI mice from the MSN-NGR1-CD11b antibody nanoparticle group were lower (Fig. 3D–H). Compared with MI group, a single administration of NGR1 without nanoparticles, both intragastric administration and intravenous injection, cannot increase the EF value. Indeed, the EF value in the group of MSN-NGR1-CD11b nanoparticles was much higher than that in the two groups of regular NGR1 treatment without nanoparticles (Fig. 3I). In addition, the expression of calcium handling proteins was detected as they are fundamental in heart repair after MI. MSN-NGR1-CD11b nanoparticles treatment significantly promoted the expression of SERCA2a (Fig. S4A), the major regulator of calcium concentration in cardiac muscles. However, as shown in Fig. S4B, no significant alterations of *p*-PLN protein levels were observed after the treatment of MSN-NGR1-CD11b antibody nanoparticles.

### 4.4. Injection of MSN-NGR1-CD11b antibody nanoparticles decrease myocardial tissue apoptosis

Cardiomyocyte apoptosis is associated with decreased cardiac function after MI. Therefore, the number of apoptotic cells in the infarct area was determined using TUNEL staining. The number of apoptotic cells was significantly lower in the MI + MSN-NGR1-CD11b antibody nanoparticle group than in the MI and MSN-NGR1 groups (Fig. 4A and B). To evaluate the type of apoptotic cells, cardiomyocytes or vascular endothelial cells were detected through immunofluorescence staining of

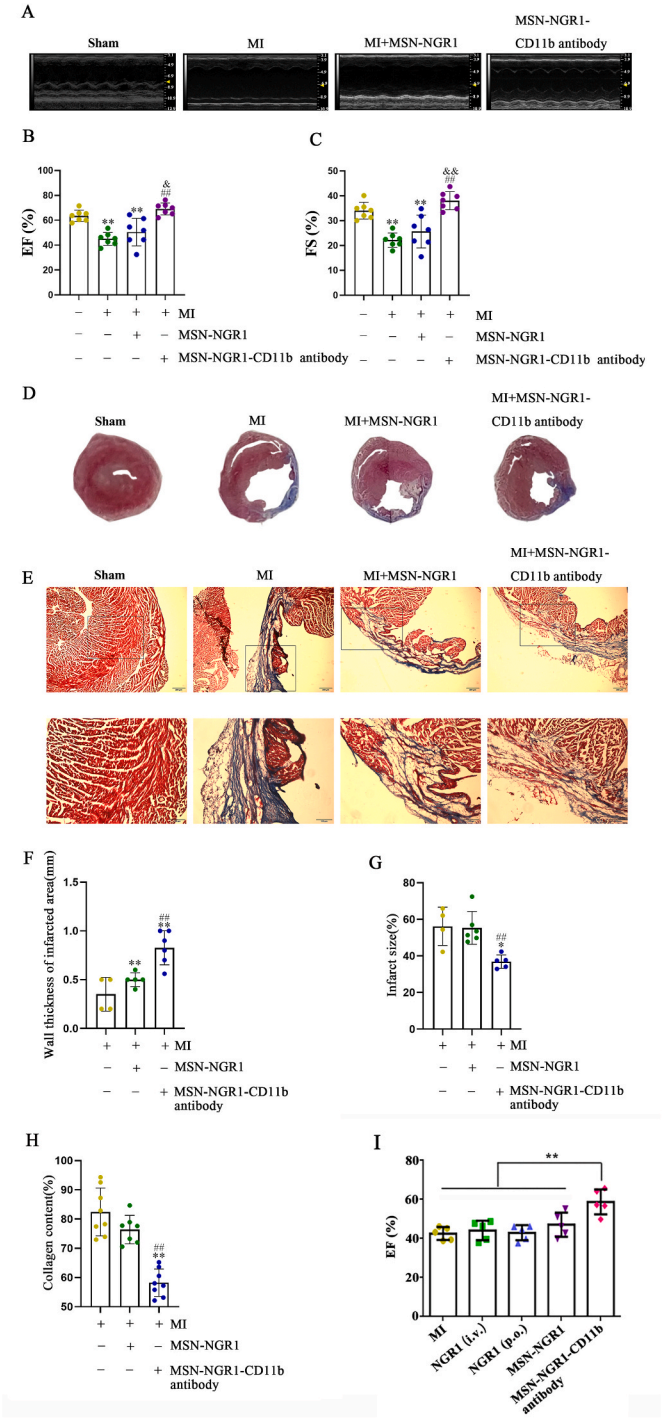


**Fig. 3.** MSN-NGR1-CD11b antibody nanoparticles administered intravenously improve cardiac function in the mouse after MI. Mouse echocardiography results (A–C). $^{**}P < 0.01$ versus the Sham group; $^{\#\#}P < 0.01$ versus the MI group; $^{\&}P < 0.05$ and $^{\&\&}P < 0.01$ versus the MI + MSN-NGR1 group. Statistical analysis of Masson's trichrome staining (D–H). Scale bar: 200 μm (E, upper panel) or 100 μm (E, lower panel). $^{*}P < 0.05$ and $^{**}P < 0.01$ versus the MI group; $^{\#\#}P < 0.01$ versus the MI + MSN-NGR1 group. Comparation of the cardioprotective effects between MSN-NGR1-CD11b nanoparticles and regular NGR1 treatment without nanoparticles (I). i.v. Indicates intravenous injection, p.o. Indicates intragastric administration. $^{**}P < 0.01$.

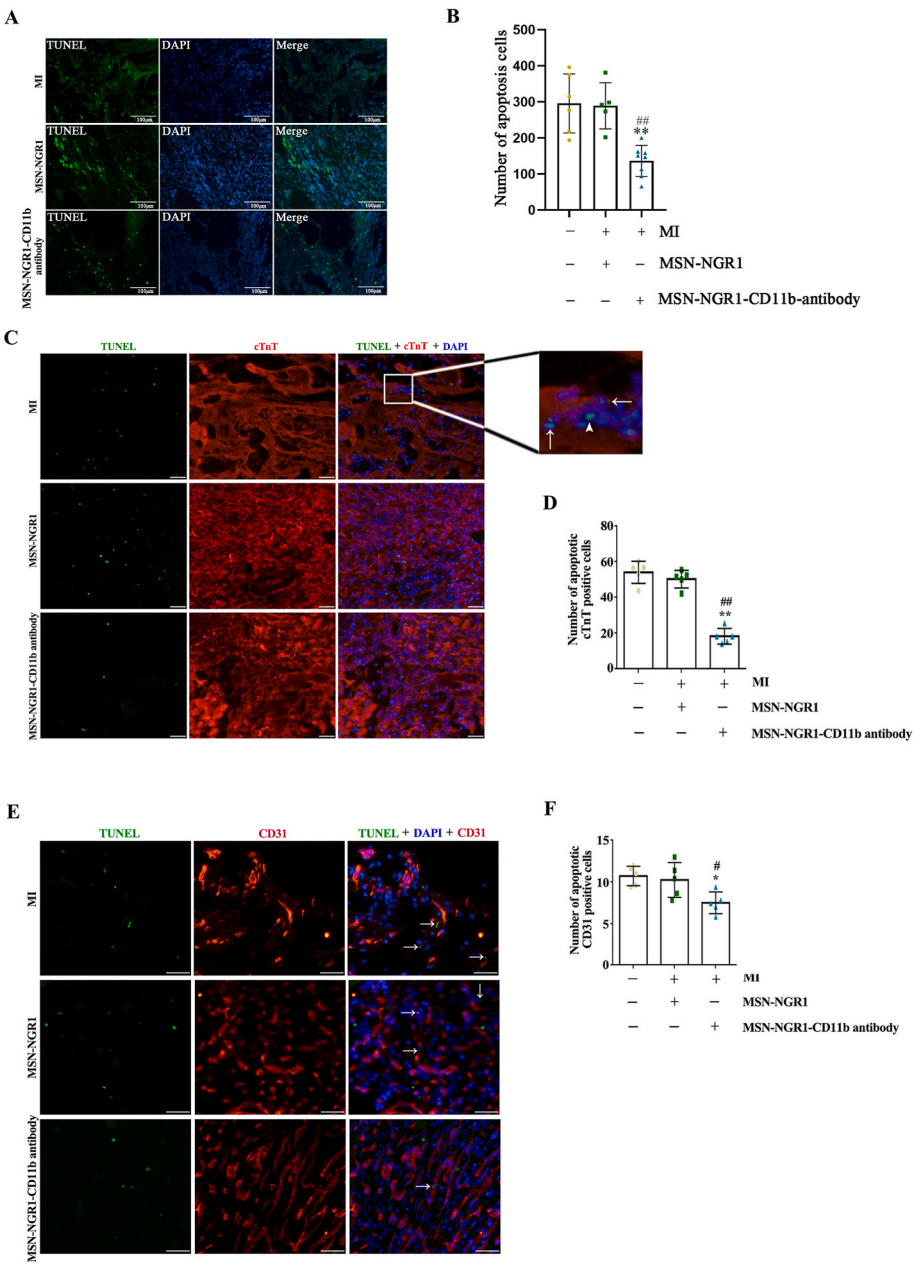


**Fig. 4.** MSN-NGR1-CD11b antibody nanoparticles injected intravenously reduce myocardial tissue apoptosis. The number of apoptotic cells in each group of infarct area was detected using the TUNEL assay approach (A, B). Scale bar: 100 μm $^{**}P < 0.01$ versus the MI group; $^{\#\#}P < 0.01$ versus the MI + MSN-NGR1 group. TUNEL staining with immunofluorescence staining of cTnT or CD31 to evaluate the type of apoptotic cells (C–F). Scale bar: 25 μm. The cell apoptosis could be occurred in cardiomyocytes (arrows, C), vascular endothelial cells (E) or other cell types (arrowhead, C). $^{*}P < 0.05$ and $^{**}P < 0.01$ versus the MI group; $^{\#}P < 0.05$ and $^{\#\#}P < 0.01$ versus the MI + MSN-NGR1 group.

cTnT or CD31. The apoptosis could be seen in cardiomyocytes, vascular endothelial cells and other cells. However, the number of apoptotic cardiomyocytes and vascular endothelial cells in MI mice from the MSN-NGR1-CD11b antibody nanoparticle group were lower than that in the MI and MSN-NGR1 groups (Fig. 4C–F).

### *4.5. Injection of MSN-NGR1-CD11b antibody nanoparticles regulate macrophage phenotype and inflammatory factors and chemokines*

NGR1 exhibits several pharmacological properties, including inhibiting inflammatory responses and oxidative stress. Considering this, we next detected whether NGR1 could change the macrophage phenotype and secretion of inflammatory factors after targeted delivery. The number of Arg-1 and CD206 positive cells was higher in the MI + MSN-NGR1-CD11b antibody nanoparticle group than in the MI and MSN-NGR1 groups at 3 days after injection (Fig. 5A–D). Besides, compared to the MI and MSN-NGR1 groups, MSN-NGE1-CD11b antibody nanoparticle injection decreased the number of CD86 positive cells (Fig. 5E and F), which indicating that the treatment of MSN-NGE1-CD11b antibody nanoparticle not only elevated the number of M2 macrophage, but also reduced the number of M1 macrophage. In addition, IL-10 expression in injured myocardium of MI + MSN-NGR1-CD11b antibody nanoparticle group was higher than that in the MI and MSN-NGR1 groups (Fig. 5G), while the IL-1β, TNF-α, and IL-6 levels were lower than those in the other two groups (Fig. 5H–J). Moreover, besides the inflammatory factors, compared to the MI and MSN-NGR1 groups, MSN-NGE1-CD11b antibody nanoparticle injection down-regulated the level of chemokine MCP-1 and up-regulated the levels of chemokines SCF and SDF-1 (Fig. 5K-M). SCF and SDF-1 not only were benefit to the survival of cardiomyocytes, but also may play an important role in the stem cell migration and recruitment after MI.

### *4.6. Injection of MSN-NGR1-CD11b antibody nanoparticles promote angiogenesis*

To further illustrate the beneficial therapeutic effects of the prepared

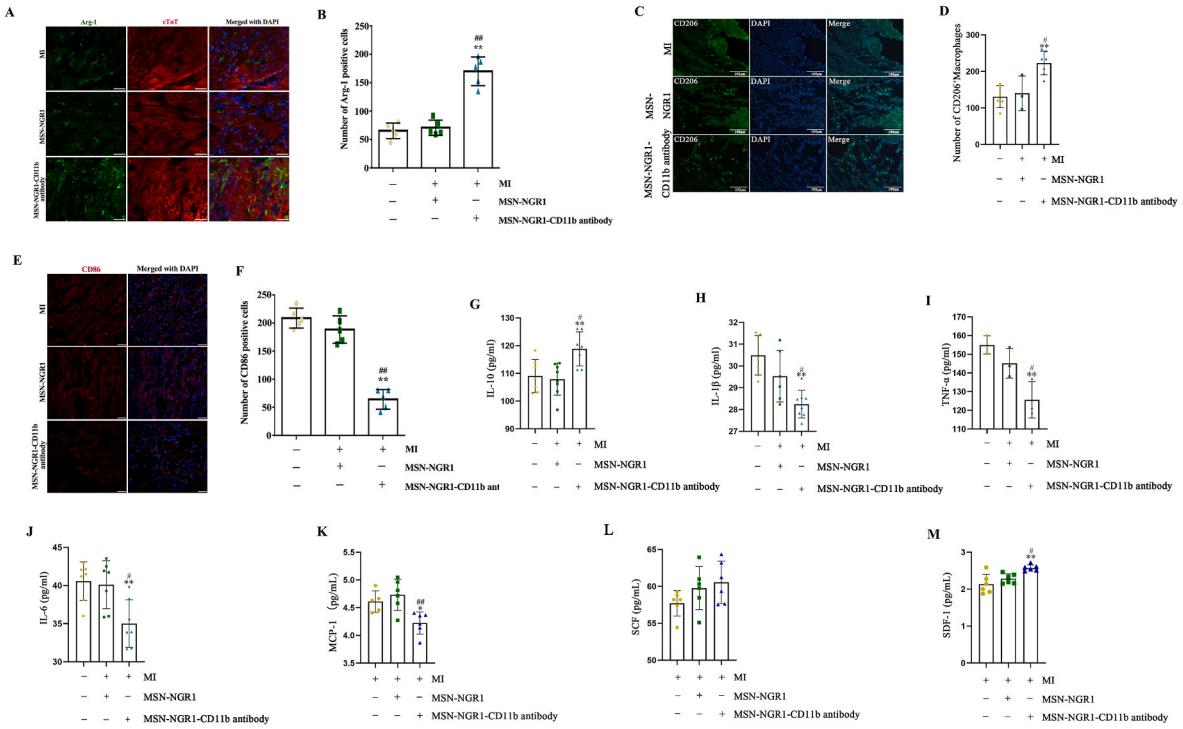


**Fig. 5.** Tail vein injection of MSN-NGR1-CD11b antibody nanoparticles induce polarization of myocardial M2 macrophages and reduce inflammation. Immunofluorescence detection of the number of Arg-1 or CD206-positive cells at the infarct site (A–D). Scale bar: 25 μm (A) or 100 μm (C). $^{**}P < 0.01$ versus the MI group; $^{\#}P < 0.05$, $^{\#\#}P < 0.01$ versus the MI + MSN-NGR1 group. Immunofluorescence detection of the number of CD86-positive cells at the infarct site (E, F). Scale bar: 25 μm. The expression of inflammatory factors and chemokines at the site of myocardial infarction was detected by ELISA (G–M). $^{*}P < 0.05$ and $^{**}P < 0.01$ versus the MI group; $^{\#}P < 0.05$, $^{\#\#}P < 0.01$ versus the MI + MSN-NGR1 group.

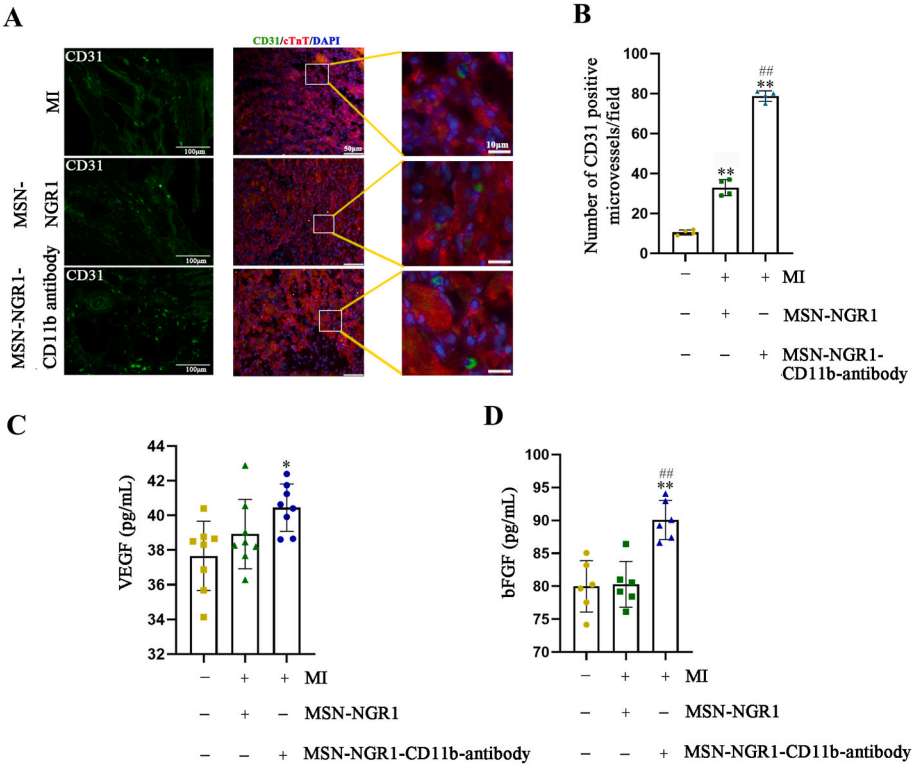


**Fig. 6.** MSN-NGR1-CD11b antibody nanoparticles injected intravenously promote angiogenesis. Immunofluorescence detection of the number of CD31-positive cells at the infarct site (A, B). Scale bar: 100 μm (left), 50 μm (right) and 10 μm (magnification). $^{**}P < 0.01$ versus the MI group; $^{\#\#}P < 0.01$ versus the MI + MSN-NGR1 group. MSN-NGR1-CD11b antibody nanoparticles increased the expression of VEGF and bFGF according to ELISA assay (C, D). $^{*}P < 0.05$, $^{**}P < 0.01$ versus the MI group; $^{\#\#}P < 0.01$ versus the MSN-NGR1 group.

nanoparticles after MI, the number of CD31 positive cells in the infarct area in the MSN-NGR1 and MSN-NGR1-CD11b groups was increased compared to that in the MI group. There was a significant difference in the number of CD31 positive cells number between the MSN-NGR1 and MSN-NGR1-CD11b antibody groups (Fig. 6A and B). Moreover, cardiac VEGF expression was higher in the MSN-NGR1-CD11b antibody group than in the MSN-NGR1 group (Fig. 6C). Compared to the MI group, cardiac bFGF levels were increased in the MSN-NGR1 and MSN-NGR1-CD11b groups. In addition, the expression of bFGF was higher in the MSN-NGR1-CD11b group than that in the MSN-NGR1 group (Fig. 6D). The elevated level of VEGF and bFGF might explain the angiogenesis enhanced by MSN-NGE1-CD11b antibody nanoparticle.

### 4.7. The NGR1-target-MI network construction

In order to further explore the mechanism of NGR1 protecting myocardium, the network pharmacology and molecular docking analyses were performed. A total of 326 non-repeating NGR1 targets and 2347 MI related genes were retrieved from the online databases. We found that 98 overlapping genes were potential targets of NGR1 against MI. These genes were imported into the STRING and then Cytoscape with nodes of NGR1 and MI to construct the NGR1-Target-MI network, which consisted of 96 nodes and 1548 edges (Fig. 7 A-a). All detailed information mentioned above were in Supplementary File S1–S4.

### 4.8. The PPI network and core PPI network of NGR1 against MI

The primary PPI network of NGR1 against MI contained 4072 nodes and 95,527 edges (Fig. 7 A-b). The detailed topology parameters of the network were shown in Supplementary File S5 Table 1. Then DC > 81 was selected as the filter criteria to generate the secondary PPI network that included 676 nodes and 29,092 edges (Fig. 7 A-c and Supplementary File S5 Table 2). Finally, according to BC > 600 filter criteria, resulting in a core PPI network with 162 nodes and 4174 edges (Fig. 7 A-d). Genes in the core PPI network (Supplementary File S5 Table 3) were considered to be the main genes directly or indirectly affected by NGR1 and mediate its antagonistic effect against MI.

### 4.9. The GO and KEGG analysis results of the core PPI network genes

GO analysis and KEGG enrichment were used for further revealing the possible mechanisms of therapeutic effects of NGR1. A total of 2447 significance items ($P < 0.05$) were obtained from GO functional analysis (Supplementary File S6), including 2064 biological process (BP) items, 184 cellular component (CC) items and 199 molecular function (MF) items. Wherein, BP items of cellular response to oxidative stress, response to oxidative stress, cellular response to reactive oxygen species, Stress-activated MAPK cascade, activation of MAPK activity were significantly enriched. A total of 132 signaling pathways were significantly enriched by KEGG analysis ($P < 0.05$). These signaling pathways (Supplementary File S7) included PI3K-Akt signaling pathway, MAPK signaling pathway, Hippo signaling pathway, FoxO signaling pathway, HIF-1 signaling pathway, Apoptosis, Signaling pathways regulating pluripotency of stem cells, Mitophagy - animal, Wnt signaling pathway and Notch signaling pathway, etc. These significantly enriched BP items and signaling pathways mentioned above were visualized, and the biological processes or pathways of interest in this study were written big red letters (Fig. 7 B). As oxidative stress is an important cause of myocardial ischemic injury, studies have shown that PI3K-Akt signaling Pathway and MAPK signaling Pathway played an important role in regulating cellular oxidative stress and maintaining cell survival. Among these items, genes AKT1 and MAPK1 (ERK2) had higher enrichment frequency, so we hypothesized that NGR1 could regulate oxidative stress through the AKT-ERK signaling pathway to alleviate myocardial cell death induced by MI.

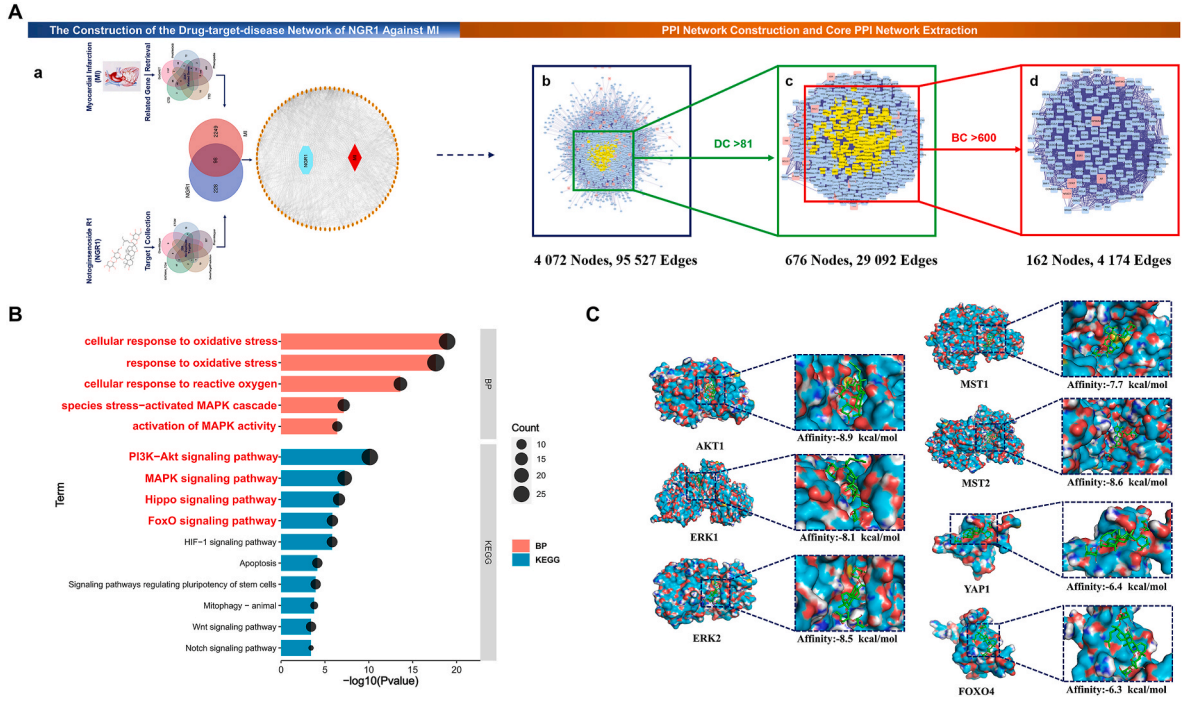


**Fig. 7.** Possible mechanism analysis and virtual validation of NGR1 against MI. **A.** Identification of core candidate targets of NGR1 against MI. **(a)** The NGR1-target-MI network construction. **(b)** The primary PPI network of NGR1 against MI. **(c)** The secondary PPI network of NGR1 against MI. **(d)** The core PPI network of NGR1 against MI. BC, betweenness centrality; DC, degree centrality. **B.** Gene ontology and KEGG enrichment of core PPI candidate targets of NGR1 against MI. Part of the items with *P* Value < 0.05 were visualized. Terms written in red were items of interest in this study. **C.** Molecular docking of the NGR1 with AKT1, ERK1, ERK2, MST1, MST2, YAP1 and FoxO4. The NGR1 was shown in stick mode. The receptor was shown in surface model. (For interpretation of the references to color in this figure legend, the reader is referred to the Web version of this article.)

### 4.10. Molecular docking of NGR1 with the key protein of AKT-ERK signaling pathway

The AKT1 (3QKK), ERK1 (2ZOQ), ERK2 (6OPH), MST1 (3COM), MST2 (4LG4), YAP1 (1JMQ) and the DNA binding domain of FOXO4 (1E17) structures files were downloaded from RCSB PDB. Binding to receptors is a prerequisite for the biological function of ligands [24]. The results of molecular docking showed that except the YAP1 (−6.4 kcal/mol) and FOXO4(−6.3 kcal/mol) the binding energies of NGR1 and AKT1, ERK1/2 and MST1/2 were all ≤ -7.0 kcal/mol, indicated that NGR1 had strong binding ability with them (Fig. 7 C). Combined with the above GO and KEGG analysis results, it was suggested that the regulation of oxidative stress mediated by AKT-ERK1/2 signaling pathway or Hippo signaling pathway may be the important mechanisms of NGR1 against MI.

### 4.11. NGR1 promotes H9C2 cell proliferation and protects H9C2 cells from $H_2O_2$-induced oxidative stress damage

After the network pharmacology and molecular docking analyses, the mechanisms of NGR1 protecting myocardium were elucidated *in vitro*. Therefore, we first pretreated different concentrations of NGR1 in H9C2 cell culture and found that NGR1 at a concentration of 100 μmol/L had the best proliferative effect (Fig. 8A–C, Fig. S5). To simulate the ischemic-hypoxic microenvironment after MI, an *in vitro* cellular oxidative stress injury model was established in H9C2 cells using 350 μmol/L $H_2O_2$ (Fig. 8D). We found that 100 μmol/L NGR1 protected H9C2 cells from $H_2O_2$-induced oxidative stress injury according to the results of the CCK8 assay (Fig. 8E). Thus, NGR1 at a concentration of 100 μmol/L and $H_2O_2$ at 350 μmol/L was chosen for subsequent cell experiments.

The number of apoptotic cells in the $H_2O_2$ intervention group increased by approximately 50%; however, the number of apoptotic H9C2 cells was significantly reduced (by approximately 16%) after pretreatment with 100 μmol/L NGR1 for 30 min. These results further validated the protective effect of NGR1 (Fig. 8F and G).

In addition, the intensity of the ROS fluorescence signal increased after $H_2O_2$ treatment in H9C2 cells, while the intensity of the ROS fluorescence signal decreased after NGR1 treatment (Fig. 8H and I). At the same time, compared to $H_2O_2$ intervention alone, the global cellular superoxide dismutase (SOD) values in the NGR1 group were significantly increased (Fig. 8J). To provide further evidence in evaluating effects of NGR1 against oxidative stress, mitochondrial ROS and oxidative DNA damage were assessed as well. After being treated by $H_2O_2$, mitochondrial ROS was extensively accumulated and oxidative damage to DNA was obvious. However, NGR1 significantly reduced mitochondrial ROS accumulation and oxidative DNA damage (Fig. 8K-N). JC-1 staining was used to detect the mitochondrial membrane potential (Fig. 8O). When the mitochondrial membrane potential is high, JC-1 aggregates in the matrix of mitochondria to form J-aggregates, which can produce red fluorescence. When the mitochondrial membrane potential is low, JC-1 cannot aggregate in the mitochondrial matrix. At this time, JC-1 is a monomer, which can produce green fluorescence. The ratio of red to green fluorescence is often used to measure the ratio of mitochondrial depolarization. After NGR1 treatment, the ratio was much higher than that in the $H_2O_2$ group (Fig. 8P), indicating that NGR1 can resistant the decrease of mitochondrial membrane potential.

In addition, we observed the proliferative effect of OGD within 12 h in H9C2 cells and found that NGR1 protected H9C2 cells from OGD-induced injury according to the results of CCK8 assay (Fig. S6, Fig. S7A). TUNEL assay further confirmed that NGR1 decreased OGD-induced cell apoptosis of H9C2 (Figs. S7B and C). Moreover, the VEGF and bFGF levels were higher after NGR1 treatment than $H_2O_2$ intervention only (Fig. S8). This result demonstrated that although the main effect of NGR1 on H9C2 in the presence of $H_2O_2$ was anti-apoptosis,

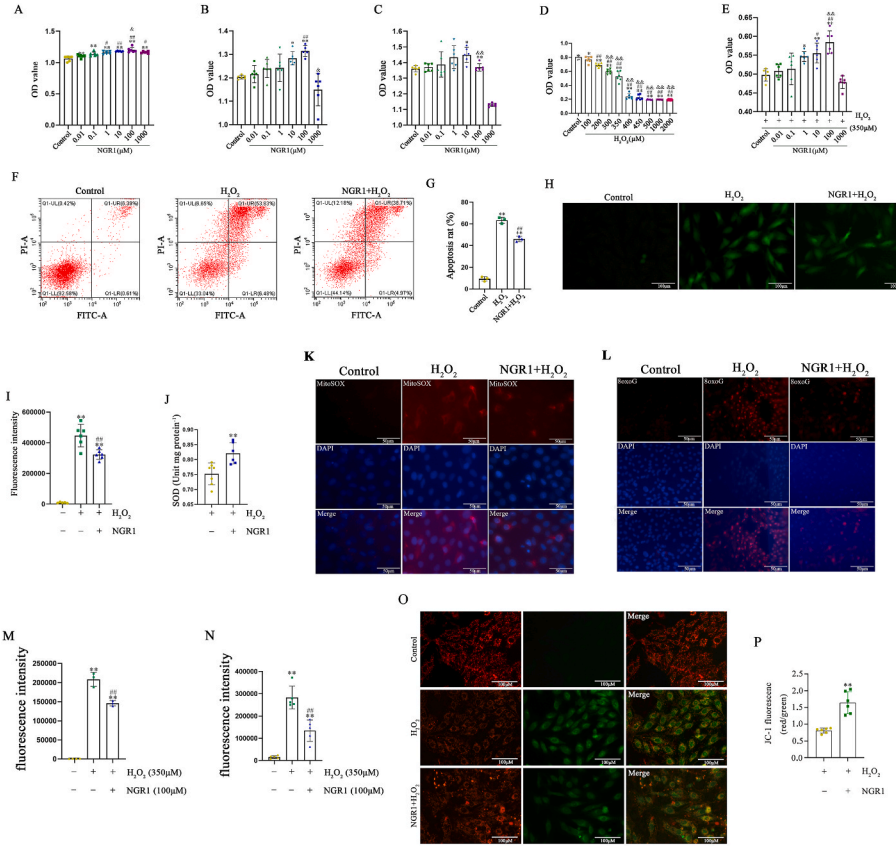


**Fig. 8.** NGR1 promotes the proliferation of H9C2 cells and protects H9C2 cells from oxidative stress induced by $H_2O_2$. Proliferation effect of NGR1 at different concentrations on H9C2 cells at 24 h, 48 h and 72 h after NGR1treatment (A–C). $^{*}P < 0.05$ and $^{**}P < 0.01$ versus the control group; $^{\#}P < 0.05$ and $^{\#\#}P < 0.01$ versus the 0.01 μM NGR1 group; $^{\&}P < 0.05$, $^{\&\&}P < 0.01$ versus the 0.1 μM NGR1 group. Damage to H9C2 cells induced by different concentrations of $H_2O_2$ (D). $^{*}P < 0.05$, $^{**}P < 0.01$ versus the control group; $^{\#\#}P < 0.01$ versus the 100 μM NGR1 group; $^{\&\&}P < 0.01$ versus the 200 μM NGR1 group. Protective effect of NGR1 against different $H_2O_2$-induced oxidative stress (E). $^{*}P < 0.05$, $^{**}P < 0.01$ versus the control group; $^{\#}P < 0.05$, $^{\#\#}P < 0.01$ versus the 0.01 μM NGR1 group; $^{\&\&}P < 0.01$ versus the 0.1 μM NGR1 group. Annexin-PI assay for the protective effect of NGR1 on H9C2 cells (F, G). $^{**}P < 0.01$ versus the control group; $^{\#\#}P < 0.01$ versus the $H_2O_2$ group. ROS assay for the protective effect of NGR1 on H9C2 cells (H, I). Scale bar: 100 μm $^{**}P < 0.01$ versus the control group; $^{\#\#}P < 0.01$ versus the $H_2O_2$ group. SOD assay for the protective effect of NGR1 on H9C2 cells (J). $^{**}P < 0.01$ versus the $H_2O_2$ group. The mitochondrial ROS and oxidative DNA damage were assessed by MitoSOX Red and 8-OxoG staining (K–N). Scale bar: 50 μm $^{**}P < 0.01$ versus the control group; $^{\#\#}P < 0.01$ versus the $H_2O_2$ group. The mitochondrial membrane potential was detected by JC-1 staining (O, P). Scale bar: 100 μm $^{**}P < 0.01$ versus the $H_2O_2$ group.

NGR1 treatment also could enhance angiogenesis through paracrine pathway, which was consistent with the results *in vivo*.

The above results showed that NGR1 significantly reduced $H_2O_2$-induced oxidative stress damage in H9C2 cells. Insulin-like growth factor (IGF-1) affects cardiovascular function in many ways, including anti-inflammatory, anti-apoptotic, and angiogenesis-stimulating. Therefore, we compared the effects of IGF-1 with those of NGR1. The CCK8 assay and TUNEL test results showed that, compared to IGF-1, $H_2O_2$-induced oxidative stress injury was reduced more significantly after NGR1 pretreatment (Figs. S9A–C). Apoptotic cells decreased by 19.72% with IGF-1, whereas the number of apoptosis in H9C2 cells was reduced by 14.80% with the addition of NGR1 (Figs. S9D and E).

### 4.12. NGR1 protects neonatal primary cardiomyocytes from $H_2O_2$ and OGD induced oxidative stress damage

As H9C2 cells are myoblasts, protective effects of NGR1 were further confirmed using neonatal primary cardiomyocytes. We found that 100 μmol/L NGR1 protected primary cardiomyocytes cells from $H_2O_2$ and OGD induced oxidative stress injury according to the results of the CCK8 assay (Fig. 9A and B). Extensive cell apoptosis was found in both $H_2O_2$ and OGD *in vitro* models. However, cell apoptosis was obviously decreased in NGR1 treatment group in the two models (Fig. 9C–F).

### 4.13. NGR1 protects adult cardiomyocytes from $H_2O_2$ induced oxidative stress damage

We further examined the cardioprotective effects of NGR1 on adult primary cardiomyocytes. According to TUNEL staining, $H_2O_2$ treatment caused plenty of apoptotic adult cardiomyocytes. However, cell apoptosis was obviously reduced in NGR1 treatment group (Fig. 10A and B). We also found that 100 μmol/L NGR1 could enhance cell viability of adult primary cardiomyocytes under $H_2O_2$ induced oxidative stress injury (Fig. 10C). The representative curves of MitoSOX Red in response to physiologic isoproterenol stimuli in adult primary cardiomyocytes were shown in Fig. 10D. The content of mitochondrial ROS was increased gradually with $H_2O_2$ treatment under isoproterenol stimuli. However, the increase in NGR1 treatment group was lower than that of $H_2O_2$ group, especially at 2 h after $H_2O_2$ treatment (Fig. 10E).

### 4.14. AKT and ERK signaling pathways were involved in protective effects of NGR1

Then, the involvement of AKT and ERK signaling pathways in cardioprotective effects of NGR1 were verified. The levels of *p*-ERK and *p*-AKT were increased following $H_2O_2$ treatment. However, NGR1 treatment further elevated the levels of *p*-ERK and *p*-AKT (Fig. 11A–C). Interestingly, NGR1 was transient (15 min) in activating the PI3K/AKT and MAPK/ERK signaling pathways (Fig. 11D–G). We performed reverse validation by pretreatment with PI3K/AKT and MAPK/ERK signaling pathway inhibitors. Cell viability was obviously decreased after LY294002 or U0126 treatment compared to that in the NGR1 group (Fig. 11H and I). TUNEL staining showed that LY294002 or U0126 treatment attenuated the protective effect of NGR1 on H9C2 against $H_2O_2$ (Fig. 11J and K), which was confirmed by flow cytometry analysis (Fig. 11L, M).

### 4.15. YAP signaling pathways were related to protective effects of NGR1

According to the network pharmacology and molecular docking analyses, not only AKT and MAPK signaling pathways were involved in the myocardial protection of NGR1, but also Hippo signaling pathway. The levels of FoxO4, p-YAP, YAP, cytoplasmic YAP and nuclear YAP were then detected. Compared with $H_2O_2$ group, NGR1 treatment decreased the expression of FoxO4 and the level of p-YAP, while increased the expression of YAP (Fig. 12A–D). The lower cytoplasmic YAP expression and higher nuclear YAP expression indicated that NGR1 could enhance YAP nuclear translocation (Fig. 12E and F). Using the immunofluorescence approach, we observed that YAP expression was dispersed in the cytoplasm of $H_2O_2$-treated cells with a faint nuclear signal, while upon NGR1 treatment, YAP signal increasingly colocalized with DAPI (Fig. 12G). In addition, whether inhibition of YAP counteracts the protective effect of NGR1 on $H_2O_2$-induced myocardial cell injury were determined. We found that inhibiting of YAP by VP, an inhibitor of

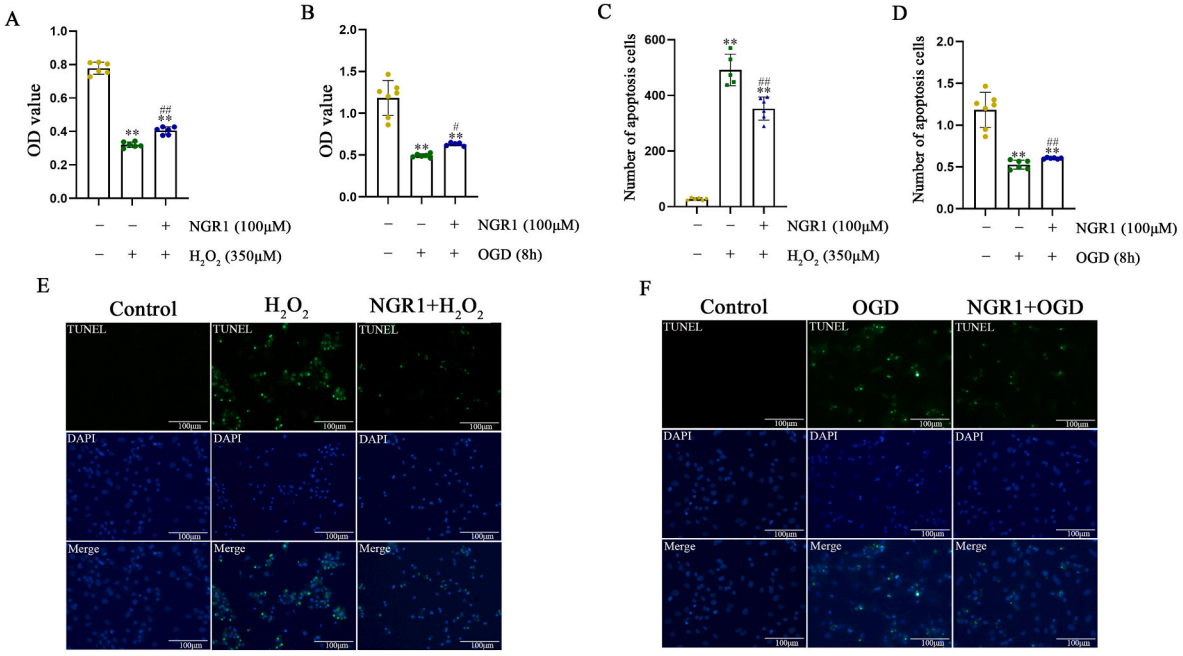


**Fig. 9.** NGR1 protects primary cardiomyocytes from oxidative stress damage induced by $H_2O_2$ and OGD. Protective effect of NGR1 on primary cardiomyocytes cells by CCK8 assay (A, B). $^{**}P < 0.01$ versus the control group; $^{\#}P < 0.05$ and $^{\#\#}P < 0.01$ versus the $H_2O_2$ group. NGR1 decreased $H_2O_2$ or OGD-induced cell apoptosis of primary cardiomyocytes according to TUNEL assay (C–F). Scale bar: 100 μm $^{**}P < 0.01$ versus the control group; $^{\#\#}P < 0.01$ versus the $H_2O_2$ or OGD group.

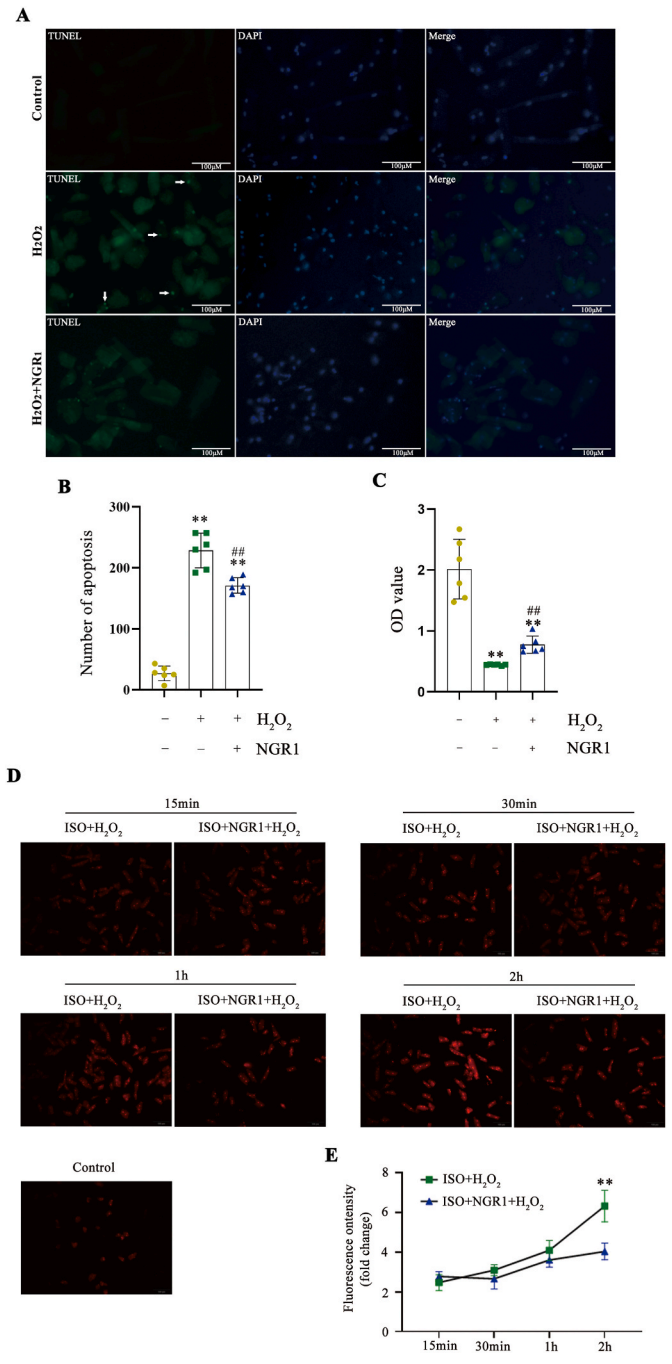


**Fig. 10.** NGR1 protects adult cardiomyocytes from $H_2O_2$ induced oxidative stress damage. NGR1 decreased $H_2O_2$-induced cell apoptosis of adult cardiomyocytes according to TUNEL assay (A, B). Scale bar: 100 μm. Protective effect of NGR1 on primary cardiomyocytes cells by CCK8 assay (C). $^{**}P < 0.01$ versus the control group; $^{\#\#}P < 0.01$ versus the $H_2O_2$ group. The representative curves of MitoSOX Red in response to physiologic isoproterenol stimuli in adult primary cardiomyocytes (D, E). Scale bar: 100 μm $^{**}P < 0.01$ versus the ISO + $H_2O_2$ group.

YAP-TEAD binding, could abrogate the protective effect of NGR1 on $H_2O_2$-induced inhibition of H9C2 cell viability (Fig. 12H). Furthermore, the results of TUNEL assay revealed that the protective effect of NGR1 on $H_2O_2$-induced H9C2 cell apoptosis was hindered following VP treatment, as indicated by the increase in number of TUNEL-positive cells (Fig. 12I and J). However, NGR1 treatment did not affect the autophagy signaling pathway (Fig. S10).

### *4.16. Intravenously injected MSN-NGR1-CD11b antibody nanoparticles activate PI3K/AKT, MAPK/ERK and YAP signaling pathways*

Finally, these mechanisms were verified in MI animals received MSN-NGR1-CD11b antibody nanoparticles. Compared to the MI and MSN-NGR1 groups, *p*-AKT and *p*-ERK protein levels in the injured myocardium of the MSN-NGE1-CD11b group were increased at 3 days after injection (Fig. 13A–D). Moreover, we found that most of *p*-AKT or *p*-AKT1/2 fluorescence signal overlapped with the cardiomyocyte marker cTnT, showing AKT and ERK1/2 pathway could be obviously activated in cardiomyocytes, which play key roles in the cardioprotective effects of MSN-NGR1-CD11b antibody nanoparticle on MI (Fig. 13E and F). After being targeted to the site of myocardial injury through MSN-NGR1-CD11b antibody nanoparticles, NGR1 obviously enhanced YAP nuclear translocation, which was conducive to the survival of cardiomyocytes (Fig. 13G). Consistent with the immunofluorescence staining, MSN-NGR1-CD11b antibody nanoparticles obviously promoted the expression of nuclear YAP and decreased the expression of cytoplasmic YAP (Fig. 13H), which further confirmed that YAP nuclear translocation was involved in the cardioprotective effects of NGR1 after being injected via the modified MSN nanoparticles. We also detected the expression of autophagy-related proteins, including Beclin-1 and LC3B. However, the injection of MSN-NGR1-CD11b antibody nanoparticles did not significantly affect the autophagy signaling pathway in the injured myocardium (Fig. S11).

## 5. Discussion

Panax ginseng has been widely used to treat cardiovascular disease because of its vasodilatory and blood pressure-lowering effects [25]. NGR1 is the main monomeric component extracted from the dried roots and rhizomes of Panax ginseng. RCT data showed that Panax ginseng administration reduced the risk of cardiovascular disease [26]. NGR1 has been approved by the Food and Drug Administration of China to conduct clinical arthritis prevention and treatment trials. However, a higher quality of evidence on clinical trial studies is highly recommended to confirm the protective effect of NGR1 on cardiac ischemia reperfusion injury in the future. NGR1 has been reported to have cardiovascular protection, neuroprotection, anti-diabetes, hepatoprotection, gastrointestinal protection, lung protection, bone metabolism regulation, renal protection, anti-cancer, and other effects [27]. The NGR1's cardiovascular protection was summarized, especially anti-apoptosis ability via MAPK, NF-kB, PI3k-AKT signaling pathways [27]. Its cardiovascular protective effects are related to oxidative stress regulation, and NGR1 can inhibit cellular oxidative stress and inflammatory response by inhibiting VEGF [28–31]. NGR1 is capable of scavenging free radicals, increasing the activity of antioxidant enzymes [32], and reducing LDH and MDA expression in the OGD environment [33,34]. Moreover, NGR1 prevents cerebral ischemia-reperfusion injury by inhibiting NADPH oxidase and mitochondria-derived superoxide and activating the AKT/Nrf2 pathway [35]. In a study on diabetic cardiomyopathy, NGR1 pretreatment significantly reduced AGE-induced mitochondrial damage, restricted ROS increase, and reduced apoptosis in H9C2 cells [36]. In oxidative stress induced osteoporpsis, NGR1 relieve oxidative stress through JNK signalling pathway [37]. Oxidized low-density lipoprotein induced oxidative stress could be alleviated by NGR1 via lnc RNA X-inactive specific transcript/miR-221 regulation [38]. NGR1 at 100 μmol/L attenuated apoptosis induced by oxygen and glucose deprivation/reoxidation [39], and also reduces MDA content and increases SOD activity in cardiomyocytes. Our research found that NGR1 pretreatment could attenuate both $H_2O_2$- and OGD-induced oxidative damage of H9C2 cells. As H9C2 cells are myoblasts, protective effects of NGR1 were further confirmed using primary cardiomyocytes. We found that NGR1 effectively protected primary cardiomyocytes cells from $H_2O_2$ and OGD induced oxidative stress injury, although the underlying mechanisms were not fully clarified.

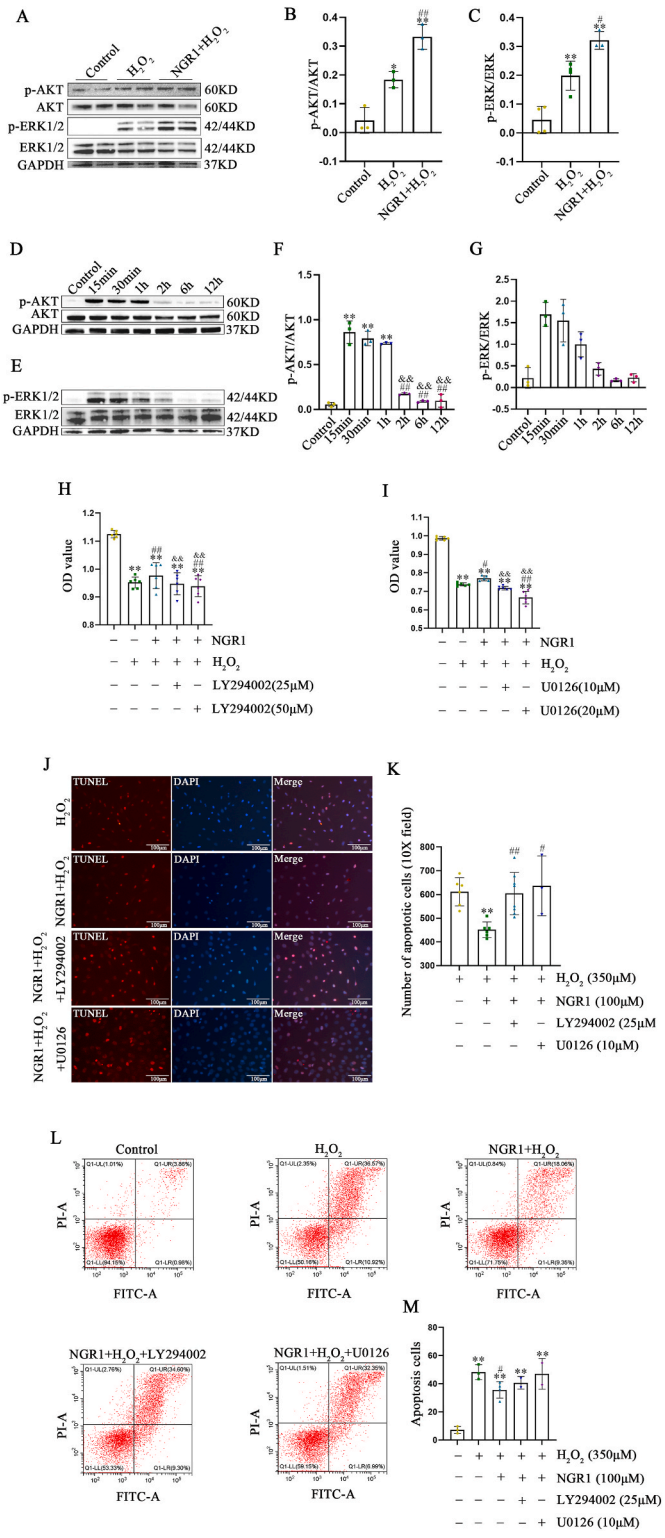


**Fig. 11.** NGR1 protects H9C2 cells from $H_2O_2$-induced cell injury through the activation of PI3K/AKT and MAPK/ERK signaling pathways. Changes in intracellular *p*-AKT and *p*-ERK1/2 protein levels after treatment of H9C2 cells with 100 μM NGR1 and 350 μM $H_2O_2$ (A–C). $^{*}P < 0.05$ and $^{**}P < 0.01$ versus the control group; $^{\#}P < 0.05$ and $^{\#\#}P < 0.01$ versus the $H_2O_2$ group. Changes in intracellular *p*-AKT and *p*-ERK levels at various time points in NGR1-treated H9C2 cells (D–G). $^{**}P < 0.01$ versus the control group; $^{\#\#}P < 0.01$ versus the 15 min group; $^{\&\&}P < 0.01$ versus the 30 min group. The protective effect of NGR1 on H9C2 cells after the addition of signaling pathway inhibitors (H, I). $^{**}P < 0.01$ versus the control group; $^{\#}P < 0.05$ and $^{\#\#}P < 0.01$ versus the $H_2O_2$ group; $^{\&}P < 0.05$ and $^{\&\&}P < 0.01$ versus the NGR1 + $H_2O_2$ group. TUNEL assay results for each group after the addition of LY294002 and U0126 (J, K). Scale bar: 100 μm $^{**}P < 0.01$ versus the $H_2O_2$ group; $^{\#}P < 0.05$, $^{\#\#}P < 0.01$ versus the NGR1 + $H_2O_2$ group. Effect of Annexin V-PI flow-through assay LY294002 and U0126 on the protective effect of NGR1 (L, M). $^{**}P < 0.01$ versus the $H_2O_2$ group; $^{\#}P < 0.05$ versus the NGR1 + $H_2O_2$ group.

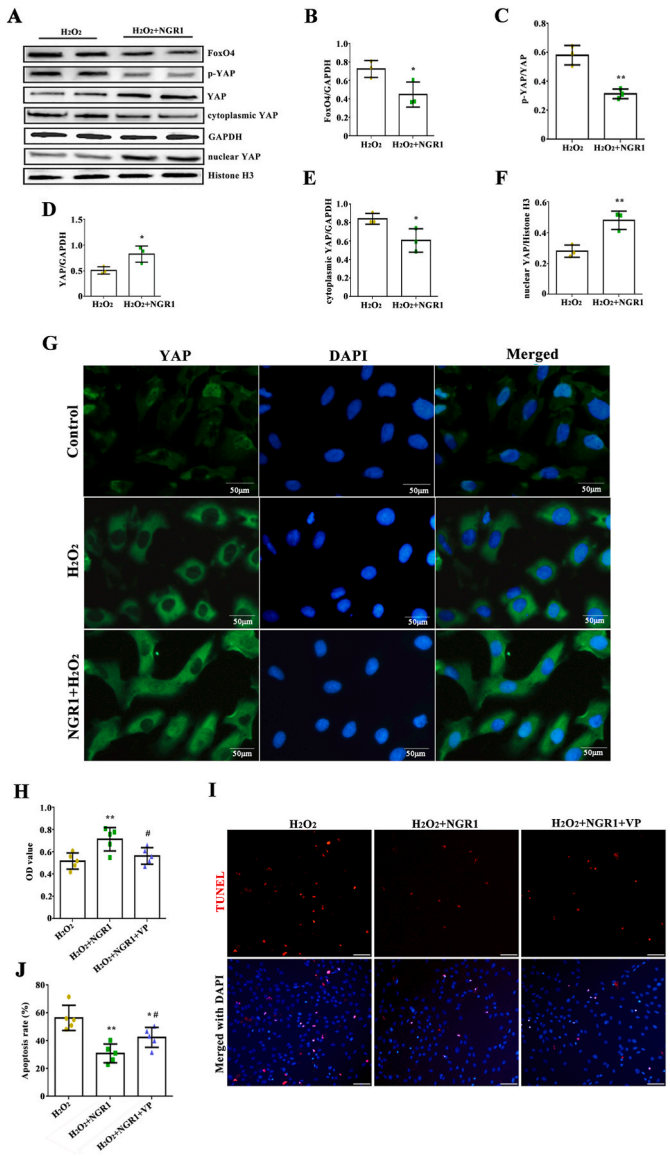


**Fig. 12.** YAP signaling pathways were involved in protective effects of NGR1. The levels of FoxO4, p-YAP, YAP, cytoplasmic YAP and nuclear YAP were detected (A–F). $^{*}P < 0.05$ and $^{**}P < 0.01$ versus the $H_2O_2$ group. Immunofluorescence staining to detect the YAP nuclear translocation (G). Scale bar: 50 μm. Inhibition of YAP by VP abrogated the protective effect of NGR1 determined by CCK8 (H) and TUNEL assay (I, J). Scale bar: 50 μm $^{*}P < 0.05$ and $^{**}P < 0.01$ versus the $H_2O_2$ group; $^{\#}P < 0.05$ versus the NGR1 + $H_2O_2$ group.

Despite the remarkable effects of NGR1 *in vitro*, previous studies have also shown that NGR1 has low bioavailability and poor permeability in the gastrointestinal tract [9,40,41], particularly in the intestinal epithelium [40]. Some researchers have used sodium *N*-[8-(2-hydroxy benzoyl) amino]octanoate (SNAC, a novel absorption enhancer) to improve the oral bioavailability of NGR [42]. Novel total saponin-loaded core-shell mixed liposome vesicles (PNS-HLV) of Panax ginseng have also been developed, and can significantly improve drug utilization and reduce brain ischemia/reperfusion (I/R)-induced cerebral infarction and brain edema [43]. Poly(d,l-propanediol) (PLGA) nanoparticles loaded with NGR1 also significantly improved pharmacokinetic activity and bioavailability [44]. Besides, sodium glycocholate (SGC)-mediated liposomes, as a nanoscale drug delivery system, were capable of significantly higher utilization of NGR1 compared to NGR1 treatment alone [45]. Therefore, it is crucial to develop a nanomaterial capable of targeting the injured heart.

Silica is widely distributed in nature and exhibits good compatibility with other materials, and has been recognized by the Food and Drug Administration as "Recognized as Safe (GRAS)" [46]. Silica nanoparticles are nanomaterials commonly used in biomedicine. It has been proven that the chemical and physical properties of nanomaterials (including particle structure, particle size, pore size and geometric shape, surface properties, and particle shape) have effects on cell uptake and intracellular translocation. In animal models, MSNs demonstrate a high degree of biocompatibility under circumstances without toxicity [47]. Owing to the unique structural properties of mesoporous particles, including their uniform pore size and pore structure, MSNs are suitable for catalysis, adsorption, separation, sensing, biomedicine, especially drug carriers [47]. Through physical or chemical modification, MSNs can reach the injured site accurately without affecting drug properties.

In the early stages of MI, myocardial tissue damage and necrosis trigger a robust inflammatory response and infiltration of immune cells such as monocytes [22]. Integral proteins distributed on the surface of these cells play an essential role in cell adhesion, migration, and signal transfer [48]. The integral protein CD11b/CD18 (also known as Mac-1, CR3, and αMβ2) is the major β2 integral protein in neutrophils, macrophages, and monocytes, which mediates the pro-inflammatory function of these cells [49,50]. In the early stages of MI, $CD11b^{+}$ cells are significantly increased, making CD11b a promising molecular target for the infarcted region of the heart after MI. We firstly directly administrated NGR1 into the local injured myocardium through inflammatory cells (especially the CD11b-expressing monocytes and neutrophils) with the help of its migration to the infarct area after MI. Therefore, we innovatively designed a MSN-conjugated CD11b antibody with loaded NGR1 (MSN-NGR1-CD11b), which allowed NGR1 precise targeted delivery to the local injured site in a noninvasively manner. Our results showed that tail vein injection of NGR1-loaded MSNs targeting CD11b-coupled antibodies in mice with MI was able to target the drug to the infarct site for release, thereby better utilizing the therapeutic effects of NGR1. We found that MSN-NGR1-CD11b antibody nanoparticle injection treatment significantly improved post-MI cardiac function, reduced post-MI infarct size and collagen deposition, prompted angiogenesis.

Increased tissue damage and a poor prognosis after MI are associated with inflammatory responses. The inflammatory response is rapidly activated within hours of MI. Macrophages can be polarized into M1 and M2 macrophages after MI, which play detrimental and beneficial roles, respectively, in wound healing. Modulation of specific macrophage phenotypes can be used therapeutically to promote myocardial repair [51,52]. In the early pro-inflammatory phase, M1 macrophages predominate in the LV, whereas M2 macrophages are predominantly increased in the infarcted area after MI. M2 macrophages play a crucial role in tissue remodeling and angiogenic response, and we found that MSN-NGR1-CD11b antibody nanoparticle injection significantly decreased the number of M1 macrophages and increased the number of M2 macrophages at the infarct site.

IL-1β, a pro-inflammatory factor, is also involved in various autoimmune inflammatory responses and multiple cellular activities [53,54]. TNF-α and IL-6 play essential regulatory roles in the myocardium of MI as major pro-inflammatory factors. TNF-α is an inflammatory cytokine produced by macrophages/monocytes during acute inflammation, and TNF-α accumulates in the heart after MI. IL-6 has multiple effects on inflammation, the immune response, and hematopoiesis [55]. IL-6 regulates the growth and differentiation of various cells, and has roles in the immune regulatory and anti-infective response [56]. Like TNF-α, the expression of IL-6 is significantly elevated during the inflammatory response phase. IL-10 is an anti-inflammatory cytokine produced by T and NK cells. Our results showed that MSN-NGR1-CD11b antibody nanoparticle injection significantly increased IL-10 secretion and significantly reduced the expression of TNF-α, IL-1β, and IL-6 at the infarction site, thus serving to balance the inflammatory response. In addition, MSN-NGE1-CD11b antibody nanoparticle injection

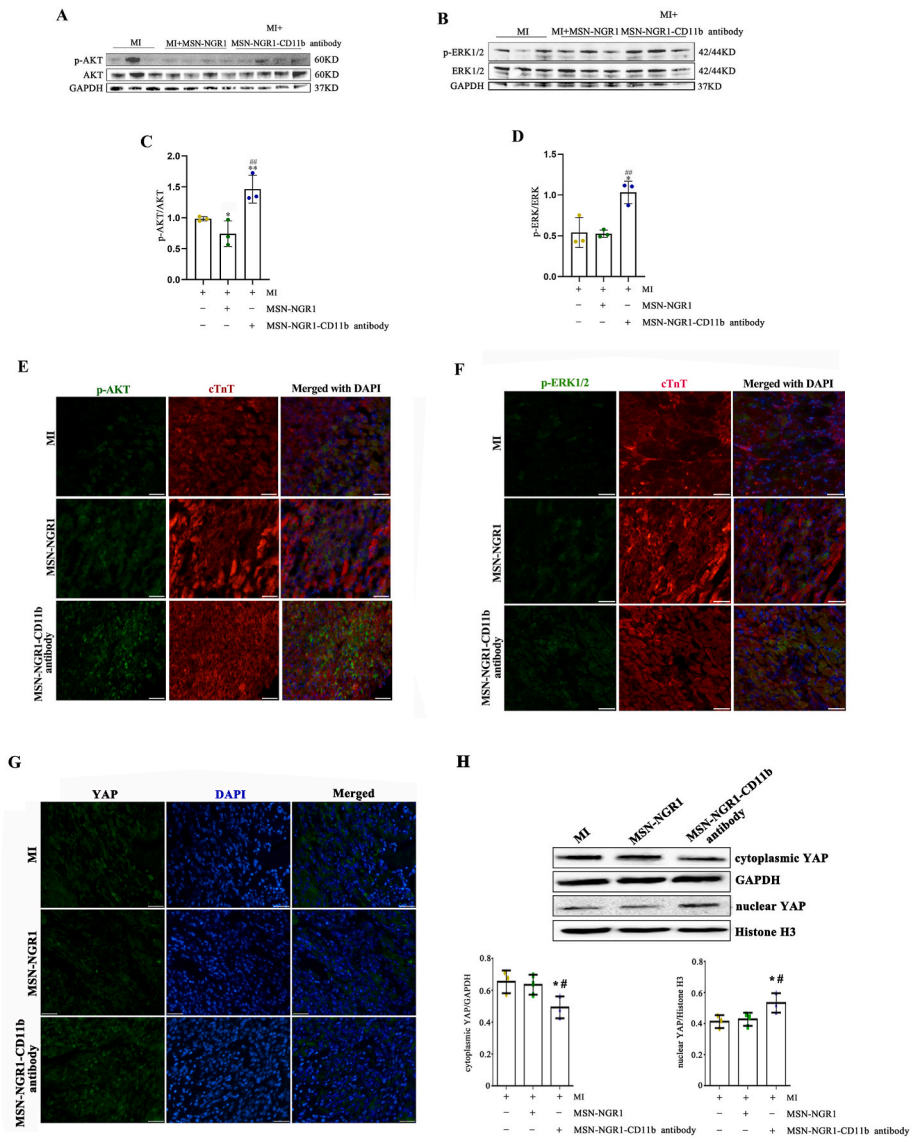


**Fig. 13.** Effect of MSN-NGR1-CD11b antibody nanoparticles injected intravenously on PI3K/AKT, ERK1/2 and YAP signaling pathways. The levels of *p*-AKT and *p*-ERK1/2 were detected by WB (A–D). $^{*}P < 0.05$, $^{**}P < 0.01$ versus the MI group; $^{\#\#}P < 0.01$ versus the MI + MSN-NGR1 group. AKT and ERK pathway could be obviously activated in cardiomyocytes according to immunofluorescence double labeling of cTnT + *p*-AKT or cTnT + *p*-ERK1/2 (E, F). Immunofluorescence staining to detect the YAP nuclear translocation (G). Scale bar: 25 μm. The levels of cytoplasmic and nuclear YAP were detected by WB (H). $^{*}P < 0.05$ versus the MI group; $^{\#}P < 0.05$ versus the MI + MSN-NGR1 group.

up-regulated the levels of chemokines SCF and SDF-1, which not only were benefit to the survival of cardiomyocytes, but also may play an important role in the stem cell migration and recruitment after MI.

Owing to the development of network pharmacology and molecular docking technology, the PI3K/AKT, MAPK and Hippo signaling pathways were focused on further elucidation of the myocardial protection mechanisms of NGR1. Cell proliferation and apoptosis are closely related to the PI3K/AKT and MAPK/ERK signaling pathways [57,58]. A previous study demonstrated that NGR1 pretreatment inhibited LPS-induced inflammatory and apoptotic responses in H9C2 cells [31], consistent with their experimental results, and found that 100 μM NGR1 administration attenuated $H_2O_2$-induced apoptosis in H9C2 cells by activating the PI3K/AKT, ERK1/2 and YAP signaling pathways. The PI3K/AKT and MAPK/ERK signaling pathways play crucial roles in MI repair. Studies have shown that AKT signaling is a potential therapeutic target for reconstituting lost mammalian cardiomyocytes [59]. Activation of the PI3K/AKT signaling pathway is also beneficial in inhibiting myocardial fibrosis after MI [60]. It has also been demonstrated that activating the MAPK/ERK signaling pathway increases angiogenesis after MI [61], while activation of the ERK signaling pathway also facilitates the maturation of reparative macrophages after MI [62]. The classic Hippo pathway plays an important role in cell proliferation, apoptosis, and differentiation. It was reported that neurofibromin 2 promoted ischemia/reperfusion injury of heart through activation of Mst1 and inhibition of YAP [63]. We also found that YAP activates phosphoinositol-3-kinase-AKT pathway through Pik3cb and regulates cardiomyocyte proliferation and survival [64], and acetylation of VGLL4 regulates Hippo-YAP signaling and postnatal cardiac growth [65]. In this study, we found that NGR1 could enhance YAP nuclear translocation in the presence of $H_2O_2$ and inhibition of YAP by VP abrogated the protective effect of NGR1. Moreover, we demonstrated that MSN-NGR1-CD11b antibody nanoparticle injection therapy also significantly activated the PI3K/AKT, MAPK/ERK and YAP signaling pathways after MI. Interestingly, these signaling pathways are all related to the redox signaling. It has been reported that calcitonin gene-related peptide regulated cardiomyocyte survival through regulation of oxidative stress by PI3K/Akt and MAPK signaling pathways [66]. Hippo/YAP is one of the crucial mediators in oxidative stress and apoptosis after MI [67]. It was reported that Hippo-YAP signaling modulated the FoxO1-mediated antioxidant response in the setting of I/R in the heart [68]. Although we found that AKT, ERK and YAP signaling pathway were involved in the cardioprotective effects of NGR1 both *in vivo* and *in vitro*, it is necessary to clarify which pathway is most important through more groupings and interventions in the future. In addition, focusing on one pathway and further investigating the NGR-1 interactions with essential factors is more helpful to demonstrate NGR-1 effects.

There were several limitations in this study. First, the interaction of MSN-CD11b antibody nanoparticles with $CD11b^+$ cells is very interesting, which should be investigated in both *in vitro* and *in vivo* settings in future study. Second, considering the pathological change after MI, we speculate that the treatment window for this strategy can be within 7 days after MI, which is a relative limited time window. Third, although we focused on AKT, ERK and YAP pathways in this study, it is interesting to further confirm other target genes from online databases. Fourth, H9C2 cardiomyoblasts show many skeletal muscle characteristics and do not have the beating function. Therefore, the cardioprotective effects of NGR1 on adult primary cardiomyocytes should be further investigated in the future. At last, taking into account sources of potential bias or imprecision because of the small sample size of this experiment, the findings in our study should be confirmed in a well-controlled study with a larger sample size and in larger animals.

In this study, MSNs coupled with CD11b antibody and loaded with NGR1 were successfully prepared, and MSN-NGR1-CD11b antibody nanoparticles improved the targeting of NGR1 to the site of MI after injection. NGR1 effectively protected H9C2 and primary cardiomyocytes cells from $H_2O_2$ and OGD induced oxidative stress injury. MSN-NGR1-CD11b antibody nanoparticles ameliorated local inflammation and promoted angiogenesis in the injured myocardium, leading to improved cardiac function after MI through enhancing the activation of AKT and MAPK signaling pathways and the nuclear translocation of YAP. This study provides a novel method for a myocardial-targeting drug delivery system with MSNs and the development of new research strategies for other biomaterials targeting the myocardium.

## Author contributions

Han Li, Jing Zhu, Yan-wu Xu, and Guo-hong Cui participated in the study design and execution, data collection, and manuscript writing; Han Li, Fang-fang Mou, Qiang-li Wang, Ya-chao Wang, and Jin-xia Mi participated in the study execution, data collection, and analysis; Jing Zhu, Bao-nian Liu, and Xiaohui Wei provided technical assistance and contributed to article editing; Yan-wu Xu, Xiao-li Shan, Shui-jin Shao, Ke Ning and Guo-hong Cui provided technical support; Rong Lu and Hai-dong Guo contributed to the study design; Hai-dong Guo contributed to the supervision of study execution, funding acquisition, and final article approval.

## Competing financial interests

The authors declare no competing financial interests.

## Foundation

This work was supported by grants from the National Natural Science Foundation of China (82174120, 81970991), Natural Science Foundation of Shanghai (No. 21ZR1463100), and the Shanghai Talent Development Funding Scheme (No. 2019090).

## Appendix A. Supplementary data

Supplementary data to this article can be found online at https://doi.org/10.1016/j.redox.2022.102384.

## References

[1] X.J. Han, H. Li, C.B. Liu, Z.R. Luo, Q.L. Wang, F.F. Mou, H.D. Guo, Guanxin Danshen Formulation improved the effect of mesenchymal stem cells transplantation for the treatment of myocardial infarction probably via enhancing the engraftment, Life Sci. 233 (2019), 116740.
[2] D. Kumar, B.I. Jugdutt, Apoptosis and oxidants in the heart, J. Lab. Clin. Med. 142 (5) (2003) 288–297.
[3] E. Murphy, C. Steenbergen, Mechanisms underlying acute protection from cardiac ischemia-reperfusion injury, Physiol. Rev. 88 (2) (2008) 581–609.
[4] X.H. Wang, G.P. Li, W.S. Yang, Z.Q. Jiao, H.M. Liu, Y.P. Ni, Cardioprotective effects of traditional Chinese medicine Guanmaitong on acute myocardial infarction, Exp. Ther. Med. 12 (6) (2016) 3927–3933.
[5] D.P. Xu, D.Z. Zou, H.L. Qiu, H.L. Wu, Traditional Chinese medicine ShenZhuGuanXin granules mitigate cardiac dysfunction and promote myocardium angiogenesis in myocardial infarction rats by upregulating PECAM-1/CD31 and VEGF expression, Evid. Based Complement. Alternat. Med. 2017 (2017), 5261729.
[6] X. Li, J. Zhang, J. Huang, A. Ma, J. Yang, W. Li, Z. Wu, C. Yao, Y. Zhang, W. Yao, B. Zhang, R. Gao, A multicenter, randomized, double-blind, parallel-group, placebo-controlled study of the effects of qili qiangxin capsules in patients with chronic heart failure, J. Am. Coll. Cardiol. 62 (12) (2013) 1065–1072.
[7] L. Tao, S. Shen, S. Fu, H. Fang, X. Wang, S. Das, J.P. Sluijter, A. Rosenzweig, Y. Zhou, X. Kong, J. Xiao, X. Li, Traditional Chinese Medication Qiliqiangxin attenuates cardiac remodeling after acute myocardial infarction in mice, Sci. Rep. 5 (2015) 8374.
[8] H.H. Pang, M.Y. Li, Y. Wang, M.K. Tang, C.H. Ma, J.M. Huang, Effect of compatible herbs on the pharmacokinetics of effective components of Panax notoginseng in Fufang Xueshuantong Capsule, J. Zhejiang Univ. - Sci. B. 18 (4) (2017) 343–352.
[9] H. Liu, J. Yang, F. Du, X. Gao, X. Ma, Y. Huang, F. Xu, W. Niu, F. Wang, Y. Mao, Y. Sun, T. Lu, C. Liu, B. Zhang, C. Li, Absorption and disposition of ginsenosides after oral administration of Panax notoginseng extract to rats, Drug Metab. Dispos. 37 (12) (2009) 2290–2298.
[10] S. Lanone, J. Boczkowski, Biomedical applications and potential health risks of nanomaterials: molecular mechanisms, Curr. Mol. Med. 6 (6) (2006) 651–663.
[11] W.J. Mulder, G.J. Strijkers, G.A. van Tilborg, D.P. Cormode, Z.A. Fayad, K. Nicolay, Nanoparticulate assemblies of amphiphiles and diagnostically active materials for multimodality imaging, Acc. Chem. Res. 42 (7) (2009) 904–914.
[12] S.K. Sahoo, V. Labhasetwar, Nanotech approaches to drug delivery and imaging, Drug Discov. Today 8 (24) (2003) 1112–1120.
[13] O.C. Farokhzad, R. Langer, Nanomedicine: developing smarter therapeutic and diagnostic modalities, Adv. Drug Deliv. Rev. 58 (14) (2006) 1456–1459.
[14] S.D. Caruthers, S.A. Wickline, G.M. Lanza, Nanotechnological applications in medicine, Curr. Opin. Biotechnol. 18 (1) (2007) 26–30.
[15] Y. Hu, J. Wang, Z. Zhi, T. Jiang, S. Wang, Facile synthesis of 3D cubic mesoporous silica microspheres with a controllable pore size and their application for improved delivery of a water-insoluble drug, J. Colloid Interface Sci. 363 (1) (2011) 410–417.
[16] F. Balas, M. Manzano, M. Colilla, M. Vallet-Regí, L-Trp adsorption into silica mesoporous materials to promote bone formation, Acta Biomater. 4 (3) (2008) 514–522.
[17] Y. Wang, Q. Zhao, Y. Hu, L. Sun, L. Bai, T. Jiang, S. Wang, Ordered nanoporous silica as carriers for improved delivery of water insoluble drugs: a comparative study between three dimensional and two dimensional macroporous silica, Int. J. Nanomed. 8 (2013) 4015–4031.
[18] S.P. Hudson, R.F. Padera, R. Langer, D.S. Kohane, The biocompatibility of mesoporous silicates, Biomaterials 29 (30) (2008) 4045–4055.
[19] Y. Zhang, J. Wang, X. Bai, T. Jiang, Q. Zhang, S. Wang, Mesoporous silica nanoparticles for increasing the oral bioavailability and permeation of poorly water soluble drugs, Mol. Pharm. 9 (3) (2012) 505–513.
[20] J. Lu, M. Liong, Z. Li, J.I. Zink, F. Tamanoi, Biocompatibility, biodistribution, and drug-delivery efficiency of mesoporous silica nanoparticles for cancer therapy in animals, Small 6 (16) (2010) 1794–1805.
[21] J.M. Miller, N.M. Mardhekar, D. Pretorius, P. Krishnamurthy, N.S. Rajasekaran, J. Zhang, R. Kannappan, DNA damage-free iPS cells exhibit potential to yield competent cardiomyocytes, Am. J. Physiol. Heart Circ. Physiol. 318 (4) (2020) H801–h815.
[22] S.D. Prabhu, N.G. Frangogiannis, The biological basis for cardiac repair after myocardial infarction: from inflammation to fibrosis, Circ. Res. 119 (1) (2016) 91–112.
[23] F.A. Azri, J. Selamat, R. Sukor, N.A. Yusof, N.H.A. Raston, S. Eissa, M. Zourob, R. Chinnappan, Determination of minimal sequence for zearalenone aptamer by computational docking and application on an indirect competitive electrochemical aptasensor, Anal. Bioanal. Chem. 413 (15) (2021) 3861–3872.
[24] N. Uddin, N. Ali, Z. Uddin, N. Nazir, M. Zahoor, U. Rashid, R. Ullah, A.S. Alqahtani, A.M. Alqahtani, F.A. Nasr, M. Liu, M. Nisar, Evaluation of Cholinesterase inhibitory potential of different genotypes of *Ziziphus nummularia*, their HPLC-UV, and molecular docking analysis, Molecules 25 (21) (2020) 5011.
[25] X. Yang, X. Xiong, H. Wang, J. Wang, Protective effects of panax notoginseng saponins on cardiovascular diseases: a comprehensive overview of experimental studies, Evid. Based Complement. Alternat. Med. 2014 (2014), 204840.
[26] J.L. Shergis, A.L. Zhang, W. Zhou, C.C. Xue, Panax ginseng in randomised controlled trials: a systematic review, Phytother Res. 27 (7) (2013) 949–965.
[27] H. Liu, J. Yang, W. Yang, S. Hu, Y. Wu, B. Zhao, H. Hu, S. Du, Focus on notoginsenoside R1 in metabolism and prevention against human diseases, Drug Des. Dev. Ther. 14 (2020) 551–565.
[28] P. Zhou, W. Xie, X. Meng, Y. Zhai, X. Dong, X. Zhang, G. Sun, X. Sun, Notoginsenoside R1 Ameliorates diabetic retinopathy through PINK1-dependent activation of Mitophagy, Cells 8 (3) (2019) 213.
[29] X. Meng, G. Sun, J. Ye, H. Xu, H. Wang, X. Sun, Notoginsenoside R1-mediated neuroprotection involves estrogen receptor-dependent crosstalk between Akt and ERK1/2 pathways: a novel mechanism of Nrf2/ARE signaling activation, Free Radic. Res. 48 (4) (2014) 445–460.
[30] S. Zou, M. Zhang, L. Feng, Y. Zhou, L. Li, L. Ban, Protective effects of notoginsenoside R1 on cerebral ischemia-reperfusion injury in rats, Exp. Ther. Med. 14 (6) (2017) 6012–6016.

[31] L. Zhong, X.L. Zhou, Y.S. Liu, Y.M. Wang, F. Ma, B.L. Guo, Z.Q. Yan, Q.Y. Zhang, Estrogen receptor α mediates the effects of notoginsenoside R1 on endotoxin-induced inflammatory and apoptotic responses in H9c2 cardiomyocytes, Mol. Med. Rep. 12 (1) (2015) 119–126.

[32] Y. Yu, G. Sun, Y. Luo, M. Wang, R. Chen, J. Zhang, Q. Ai, N. Xing, X. Sun, Cardioprotective effects of Notoginsenoside R1 against ischemia/reperfusion injuries by regulating oxidative stress- and endoplasmic reticulum stress- related signaling pathways, Sci. Rep. 6 (2016), 21730.

[33] Z. Liu, H. Wang, G. Hou, H. Cao, Y. Zhao, B. Yang, Notoginsenoside R1 protects oxygen and glucose deprivation-induced injury by upregulation of miR-21 in cardiomyocytes, J. Cell. Biochem. 120 (6) (2019) 9181–9192.

[34] Z. Jin, C. Gan, G. Luo, G. Hu, X. Yang, Z. Qian, S. Yao, Notoginsenoside R1 protects hypoxia-reoxygenation deprivation-induced injury by upregulation of miR-132 in H9c2 cells, Hum. Exp. Toxicol. 40 (12_suppl) (2021) S29–S38.

[35] X. Meng, M. Wang, X. Wang, G. Sun, J. Ye, H. Xu, X. Sun, Suppression of NADPH oxidase- and mitochondrion-derived superoxide by Notoginsenoside R1 protects against cerebral ischemia-reperfusion injury through estrogen receptor-dependent activation of Akt/Nrf2 pathways, Free Radic. Res. 48 (7) (2014) 823–838.

[36] B. Zhang, J. Zhang, C. Zhang, X. Zhang, J. Ye, S. Kuang, G. Sun, X. Sun, Notoginsenoside R1 protects against diabetic cardiomyopathy through activating estrogen receptor α and its downstream signaling, Front. Pharmacol. 9 (2018) 1227.

[37] X. Li, H. Lin, X. Zhang, R.T. Jaspers, Q. Yu, Y. Ji, T. Forouzanfar, D. Wang, S. Huang, G. Wu, Notoginsenoside R1 attenuates oxidative stress-induced osteoblast dysfunction through JNK signalling pathway, J. Cell Mol. Med. 25 (24) (2021) 11278–11289.

[38] J. Zhao, L. Cui, J. Sun, Z. Xie, L. Zhang, Z. Ding, X. Quan, Notoginsenoside R1 alleviates oxidized low-density lipoprotein-induced apoptosis, inflammatory response, and oxidative stress in HUVECS through modulation of XIST/miR-221-3p/TRAF6 axis, Cell. Signal. 76 (2020), 109781.

[39] K. He, L. Yan, C.S. Pan, Y.Y. Liu, Y.C. Cui, B.H. Hu, X. Chang, Q. Li, K. Sun, X. W. Mao, J.Y. Fan, J.Y. Han, ROCK-dependent ATP5D modulation contributes to the protection of notoginsenoside NR1 against ischemia-reperfusion-induced myocardial injury, Am. J. Physiol. Heart Circ. Physiol. 307 (12) (2014) H1764–H1776.

[40] F. Liang, J.X. Hua, Absorption profiles of sanchinoside R1 and ginsenoside Rg1 in the rat intestine, Eur. J. Drug Metab. Pharmacokinet. 30 (4) (2005) 261–268.

[41] J.Q. Ruan, W.I. Leong, R. Yan, Y.T. Wang, Characterization of metabolism and in vitro permeability study of notoginsenoside R1 from Radix notoginseng, J. Agric. Food Chem. 58 (9) (2010) 5770–5776.

[42] Y. Li, D. Yang, C. Zhu, Impact of sodium *N*-[8-(2-Hydroxybenzoyl)amino]-caprylate on intestinal permeability for notoginsenoside R1 and salvianolic Acids in Caco-2 cells transport and rat pharmacokinetics, Molecules 23 (11) (2018) 2990.

[43] J. Zhang, X. Han, X. Li, Y. Luo, H. Zhao, M. Yang, B. Ni, Z. Liao, Core-shell hybrid liposomal vesicles loaded with panax notoginsenoside: preparation, characterization and protective effects on global cerebral ischemia/reperfusion injury and acute myocardial ischemia in rats, Int. J. Nanomed. 7 (2012) 4299–4310.

[44] H. Cai, X. Wen, L. Wen, N. Tirelli, X. Zhang, Y. Zhang, H. Su, F. Yang, G. Chen, Enhanced local bioavailability of single or compound drugs delivery to the inner ear through application of PLGA nanoparticles via round window administration, Int. J. Nanomed. 9 (2014) 5591–5601.

[45] Q. Fan, Y. Zhang, X. Hou, Z. Li, K. Zhang, Q. Shao, N. Feng, Improved oral bioavailability of notoginsenoside R1 with sodium glycocholate-mediated liposomes: preparation by supercritical fluid technology and evaluation in vitro and in vivo, Int. J. Pharm. 552 (1–2) (2018) 360–370.

[46] A.E. Garcia-Bennett, Synthesis, toxicology and potential of ordered mesoporous materials in nanomedicine, Nanomedicine (Lond) 6 (5) (2011) 867–877.

[47] J. Wen, K. Yang, F. Liu, H. Li, Y. Xu, S. Sun, Diverse gatekeepers for mesoporous silica nanoparticle based drug delivery systems, Chem. Soc. Rev. 46 (19) (2017) 6024–6045.

[48] R.O. Hynes, Integrins: bidirectional, allosteric signaling machines, Cell 110 (6) (2002) 673–687.

[49] V. Gupta, J.L. Alonso, T. Sugimori, M. Essafi, J.P. Xiong, M.A. Arnaout, Role of the beta-subunit arginine/lysine finger in integrin heterodimer formation and function, J. Immunol. 180 (3) (2008) 1713–1718.

[50] V. Gupta, A. Gylling, J.L. Alonso, T. Sugimori, P. Ianakiev, J.P. Xiong, M. A. Arnaout, The beta-tail domain (betaTD) regulates physiologic ligand binding to integrin CD11b/CD18, Blood 109 (8) (2007) 3513–3520.

[51] M.A. Ismahil, T. Hamid, S.S. Bansal, B. Patel, J.R. Kingery, S.D. Prabhu, Remodeling of the mononuclear phagocyte network underlies chronic inflammation and disease progression in heart failure: critical importance of the cardiosplenic axis, Circ. Res. 114 (2) (2014) 266–282.

[52] M. Nahrendorf, M.J. Pittet, F.K. Swirski, Monocytes: protagonists of infarct inflammation and repair after myocardial infarction, Circulation 121 (22) (2010) 2437–2445.

[53] H.J. Anders, Of inflammasomes and Alarmins: IL-1β and IL-1α in kidney disease, J. Am. Soc. Nephrol. 27 (9) (2016) 2564–2575.

[54] H. Lin, D. Gao, M.M. Hu, M. Zhang, X.X. Wu, L. Feng, W.H. Xu, Q. Yang, X. Zhong, J. Wei, Z.S. Xu, H.X. Zhang, Z.M. Song, Q. Zhou, W. Ye, Y. Liu, S. Li, H.B. Shu, MARCH3 attenuates IL-1β-triggered inflammation by mediating K48-linked polyubiquitination and degradation of IL-1RI, Proc. Natl. Acad. Sci. U.S.A. 115 (49) (2018) 12483–12488.

[55] T. Tanaka, M. Narazaki, T. Kishimoto, IL-6 in inflammation, immunity, and disease, Cold Spring Harbor Perspect. Biol. 6 (10) (2014) a016295.

[56] K. Taniguchi, M. Karin, IL-6 and related cytokines as the critical lynchpins between inflammation and cancer, Semin. Immunol. 26 (1) (2014) 54–74.

[57] A. Samakova, A. Gazova, N. Sabova, S. Valaskova, M. Jurikova, J. Kyselovic, The PI3k/Akt pathway is associated with angiogenesis, oxidative stress and survival of mesenchymal stem cells in pathophysiologic condition in ischemia, Physiol. Res. 68 (Suppl 2) (2019) S131–S138.

[58] L. Yin, D. Huang, X. Liu, Y. Wang, J. Liu, F. Liu, B. Yu, Omentin-1 effects on mesenchymal stem cells: proliferation, apoptosis, and angiogenesis in vitro, Stem Cell Res. Ther. 8 (1) (2017) 224.

[59] L. Zhen, Q. Zhao, J. Lü, S. Deng, Z. Xu, L. Zhang, Y. Zhang, H. Fan, X. Chen, Z. Liu, Y. Gu, Z. Yu, miR-301a-PTEN-AKT signaling induces cardiomyocyte proliferation and promotes cardiac repair post-MI, Mol. Ther. Nucleic Acids 22 (2020) 251–262.

[60] W. Yang, Z. Wu, K. Yang, Y. Han, Y. Chen, W. Zhao, F. Huang, Y. Jin, W. Jin, BMI1 promotes cardiac fibrosis in ischemia-induced heart failure via the PTEN-PI3K/Akt-mTOR signaling pathway, Am. J. Physiol. Heart Circ. Physiol. 316 (1) (2019) H61–H69.

[61] S.N. Li, P. Li, W.H. Liu, J.J. Shang, S.L. Qiu, M.X. Zhou, H.X. Liu, Danhong injection enhances angiogenesis after myocardial infarction by activating MiR-126/ERK/VEGF pathway, Biomed. Pharmacother. 120 (2019), 109538.

[62] K. Shirakawa, J. Endo, M. Kataoka, Y. Katsumata, A. Anzai, H. Moriyama, H. Kitakata, T. Hiraide, S. Ko, S. Goto, G. Ichihara, K. Fukuda, T. Minamino, M. Sano, MerTK expression and ERK activation are essential for the functional maturation of osteopontin-producing reparative macrophages after myocardial infarction, J. Am. Heart Assoc. 9 (18) (2020), e017071.

[63] T. Matsuda, P. Zhai, S. Sciarretta, Y. Zhang, J.I. Jeong, S. Ikeda, J. Park, C.P. Hsu, B. Tian, D. Pan, J. Sadoshima, D.P. Del Re, NF2 activates Hippo signaling and promotes ischemia/reperfusion injury in the heart, Circ. Res. 119 (5) (2016) 596–606.

[64] Z. Lin, P. Zhou, A. von Gise, F. Gu, Q. Ma, J. Chen, H. Guo, P.R. van Gorp, D. Z. Wang, W.T. Pu, Pi3kcb links Hippo-YAP and PI3K-AKT signaling pathways to promote cardiomyocyte proliferation and survival, Circ. Res. 116 (1) (2015) 35–45.

[65] Z. Lin, H. Guo, Y. Cao, S. Zohrabian, P. Zhou, Q. Ma, N. VanDusen, Y. Guo, J. Zhang, S.M. Stevens, F. Liang, Q. Quan, P.R. van Gorp, A. Li, C. Dos Remedios, A. He, V.J. Bezzerides, W.T. Pu, Acetylation of VGLL4 regulates hippo-YAP signaling and postnatal cardiac growth, Dev. Cell 39 (4) (2016) 466–479.

[66] N.A. Umoh, R.K. Walker, R.M. Millis, M. Al-Rubaiee, P.R. Gangula, G.E. Haddad, Calcitonin gene-related peptide regulates cardiomyocyte survival through regulation of oxidative stress by PI3K/Akt and MAPK signaling pathways, Ann. Clin. Exp. Hypertens. 2 (1) (2014) 1007.

[67] Q. Zhang, L. Wang, S. Wang, H. Cheng, L. Xu, G. Pei, Y. Wang, C. Fu, Y. Jiang, C. He, Q. Wei, Signaling pathways and targeted therapy for myocardial infarction, Signal Transduct. Targeted Ther. 7 (1) (2022) 78.

[68] D. Shao, P. Zhai, D.P. Del Re, S. Sciarretta, N. Yabuta, H. Nojima, D.S. Lim, D. Pan, J. Sadoshima, A functional interaction between Hippo-YAP signalling and FoxO1 mediates the oxidative stress response, Nat. Commun. 5 (2014) 3315.